UC Berkeley
UC Berkeley Electronic Theses and Dissertations

Title

Magnetic Particle Imaging with Advanced Tomographic Reconstruction Methods

Permalink

https://escholarship.org/uc/item/0kr099fr

Author

Konkle, Justin Joseph

Publication Date

2014

Peer reviewed|Thesis/dissertation

Magnetic Particle Imaging with Advanced Tomographic Reconstruction Methods

by

Justin Joseph Konkle

A dissertation submitted in partial satisfaction of the
requirements for the degree of
Joint Doctor of Philosophy

in

Bioengineering

in the

Graduate Division

of the

University of California, Berkeley

Committee in charge:

Professor Steven M. Conolly, Chair
Professor Nola M. Hylton
Professor Seth R. Sanders

Fall 2014

Magnetic Particle Imaging with
Advanced Tomographic Reconstruction Methods

Abstract

Magnetic Particle Imaging with
Advanced Tomographic Reconstruction Methods

by

Justin Joseph Konkle

Joint Doctor of Philosophy in Bioengineering

University of California, Berkeley

Professor Steven M. Conolly, Chair

Magnetic Particle Imaging (MPI) is an emerging imaging modality with potential clinical applications in rapid angiography, cell therapy tracking, cancer imaging, and inflammation imaging. While still in its infancy, MPI already has excellent contrast, safety, depth penetration, and sensitivity without the serious health risks posed by current modalities such as ionizing radiation and iodinated contrast agents.

With any tracer imaging modality, high sensitivity is necessary to improve safety and enable new clinical applications. The first Magnetic Computed Tomography (MCT) system and experimental images were created in this work with the goal of improving sensitivity in MPI. MCT uses projection reconstruction algorithms similar to those in X-ray computed tomography to reconstruct 3D images from a projection MPI sytem. Analytical derivation and experimental evidence demonstrate that MCT has an order-of-magnitude higher SNR than previous 3D MPI methods for the same scan time as well as a 40% resolution improvement. The MCT experimental system acquisition speed was improved from initial work to acquire images twenty-fold faster at less than two minutes per 3D image.

Critical to any medical imaging technology is the reliability and accuracy of image reconstruction. Unfortunately, prior approaches to x-space MPI reconstruction suffer from image artifacts such as banding and haze. In this work, *a priori* knowledge of image continuity and non-negativity are introduced into a new optimization formulation to reduce these non-physical artifacts in 2D and 3D reconstructions.

To my family and friends

For their guidance, love, support, encouragement, and balance.

Contents

List of Figures

List of Tables

Acknowledgments

To Steve Conolly, my graduate research adviser, thank you for challenging me to improve, providing innovative ideas for my research and direction throughout my projects, giving excellent paper and presentation feedback, and always being a helpful, kind, and thoughtful adviser. Under your leadership I have become a better researcher and engineer. I greatly appreciate the skills and knowledge I gained in your lab.

To Patrick Goodwill, thank you for providing daily project guidance, support, and expertise, as well as laying the groundwork necessary for my projects to succeed.

To my lab-mates, collaborators, and co-authors, Emine Saritas, Bo Zheng, Kuan Lu, Laura Croft, Paul Keselman, Daniel Hensley, Ryan Orendorff, Elaine Yu, Robert Frawley, Oscar Carrasco-Zevallos, Nitish Padmanaban, Martin Uecker, Jon Tamir, Matt Ferguson, and Kannan Krishnan, thank you for all of your help with experiments, assistance in writing papers, excellent feedback on presentations and papers, lively discussions, and giving friendship.

To Miki Lustig, thank you for all the great ideas and insightful discussion of concepts for MPI reconstruction.

To my qualifying exam and dissertation committees, Nola Hylton, Miki Lustig, Jitendra Malik, and Seth Sanders, thank you for your time and project feedback.

To my family, thank you for your guidance, love, and support as well as instilling in me the diligence and curiosity essential to this work.

To my wife, Michelle, no amount thanks would be enough for all your patience, understanding, and giving in the past five years. Thank you for helping motivate me when necessary yet also encouraging life balance.

–

Chapter 1

Introduction

Magnetic Particle Imaging is a novel, safe, sensitive, high-contrast, and fast imaging modality [17, 77, 24, 39, 65, 66]. MPI directly detects magnetic nanoparticle tracers deep in tissue with ideal contrast for diagnostic and interventional medical imaging procedures including angiography, cell therapy tracking, cancer imaging, inflammation imaging, temperature mapping, biomarker imaging, tracking of targeted chemotherapies, and functionalized USPIOs [17, 65, 74, 62, 7, 69, 2, 11, 42, 57]. The MPI technique detects only magnetic particles and derives no signal from tissue, unlike Computed Tomography (CT) and Magnetic Resonance Imaging (MRI), which gives MPI unique contrast that is best compared with nuclear imaging but without ionizing radiation.

The physics and hardware required for MPI are completely distinct from existing medical imaging modalities, and MPI images cannot be acquired using MRI. There are several proposed modes of MPI scanning, including 3D Field Free Point (FFP) scanning [17, 77, 23, 68, 22, 21, 25], single sided systems [67], 2D projection MPI (akin to X-ray) with a Field Free Line (FFL) magnet [35, 40, 25], and 3D FFL MPI [76, 34, 12, 37, 39]. In this work, 3D FFL MPI is referred to as both projection reconstruction MPI (PR MPI) and magnetic computed tomography (MCT). To date, MPI has been demonstrated with phantom imaging experiments, as well as in mice injected intravascularly with USPIO tracers [21, 77].

MPI forms images of magnetic nanoparticle concentrations by detecting the non-linear magnetic response of a nanoparticle to applied magnetic fields. The key concept that underlies MPI is that a strong magnetic field gradient, known as a selection field, selectively saturates magnetic nanoparticles at all locations except at the "field free" region (FFR), which can be either a field free point (FFP) or a field free line (FFL) [17, 76]. A FFP selects a single point while a FFL selects a line in space. To produce a signal, an excitation electromagnet creates a rapidly time varying homogeneous magnetic field, known as a drive field, that rapidly moves the FFP or FFL. When the FFP or FFL passes over a magnetic nanoparticle, the nanoparticle magnetization flips in direction and induces a signal in a receiver coil. The spatial extent that the FFP or FFL can move using only the drive field is limited by magnetostimulation [66]. To enable scanning large regions of interest, we add slowly varying homogeneous magnetic fields [68, 22], sometimes called focus fields.

This dissertation covers efforts to improve many aspects of MPI systems including increasing MPI sensitivity, increasing system resolution, speeding scan time, and reducing image artifacts. This dissertation is a compilation of work from two peer reviewed journal papers, one conference paper, and one journal paper in preparation at the time of this writing. Each paper is contained within its own chapter which is summarized below.

Chapter 2: Development of a FFL magnet for projection MPI

The field free line (FFL) magnet has the potential to greatly increase signal to noise ratio (SNR) or to decrease scan time for magnetic particle imaging (MPI). The use of an FFL will decrease scan time by reducing image dimensionality from a 3D image to a projection image. Alternatively, in comparison to a 3D scan of equal scan time, an FFL scanner will increase SNR through more signal averages. An FFL magnet would enable projection imaging as is used in projection x-ray and is common in angiography. The Philips and Lubeck groups have pioneered the design of field free line magnets for MPI and have shown that they can achieve power efficiency similar to that of a field free point, the standard in MPI [17, 76, 34].

Current FFL magnet designs have not been optimized for characteristics such as gradient efficiency and gradient magnitude homogeneity. This work shows a 2.25 T/m Halbach quadrupole permanent magnet design that produces a homogeneous magnetic field along the field free line. Along the FFL, we experimentally measured a field maximum of 2 mT within the imaging field of view (FOV), and we experimentally measured that the gradient perpendicular to the FFL deviates by a maximum of 3.4%.

Citation:

J. Konkle, P. Goodwill, and S. Conolly, "Development of a Field Free Line Magnet for Projection MPI," in Proc. SPIE 7965, Medical Imaging 2011: Biomedical Applications in Molecular, Structural, and Functional Imaging, 2011, vol. 7965, p. 79650X-79650X-7.

Chapter 3: Projection reconstruction MPI

We acquire the first experimental 3D tomographic images with Magnetic Particle Imaging (MPI) using projection reconstruction methodology, which is similar to algorithms employed in X-ray computed tomography. The primary advantage of projection reconstruction methods is an order of magnitude increase in SNR due to averaging. We first derive the point spread function, resolution, number of projections required, and the SNR gain in projection reconstruction MPI. We then design and construct the first scanner capable of gathering the necessary data for non-aliased projection reconstruction and experimentally verify our mathematical predictions. We demonstrate that filtered backprojection in MPI is experimentally feasible and illustrate the SNR and resolution improvements with projection reconstruction. Finally, we show that MPI is capable of producing three dimensional imaging volumes in both phantoms and post-mortem mice.

Citation:

J. J. Konkle, P. W. Goodwill, O. M. Carrasco-Zevallos, and S. M. Conolly, "Projection reconstruction magnetic particle imaging.," *IEEE Trans. Med. Imaging*, vol. 32, no. 2, pp. 338-47, Feb. 2013.

Chapter 4: Twenty-fold acceleration of projection reconstruction MPI

We experimentally demonstrate a 20-fold improvement in acquisition time in projection reconstruction (PR) Magnetic Particle Imaging (MPI) relative to the state of the art PR MPI imaging results to date. We achieve this acceleration in our imaging system by introducing an additional Helmholtz electromagnet pair, which creates a slow shift (focus) field. Due to magnetostimulation limits in humans, we show that scan time with 3D PR MPI is theoretically within the same order of magnitude as 3D MPI with a field free point; however, PR MPI has an order of magnitude signal-to-noise ratio (SNR) gain.

Citation:

J. J. Konkle, P. W. Goodwill, E. U. Saritas, B. Zheng, K. Lu, and S. M. Conolly, "Twenty-fold acceleration of 3D projection reconstruction MPI.," *Biomed. Tech. (Berl).*, vol. 58, no. 6, pp. 565-76, Dec. 2013.

Chapter 5: Magnetic Particle Imaging X-space Reconstruction using Convex Optimization

Critical to any medical imaging technology is the reliability and accuracy of image reconstruction. Recent progress in x-space MPI reconstruction has demonstrated experimental linearly quantitative imaging across mouse and rat sized fields of view. Unfortunately, prior approaches to x-space MPI reconstruction suffer from image artifacts such as banding and haze. In this work we apply robust *a priori* knowledge of image continuity and non-negativity to remove non-physical banding and haze artifacts in 2D and 3D reconstructions. We conclude with a discussion of how the presented reconstruction platform is flexible to enable reconstruction of generalized excitation trajectories, projection reconstruction, and compressed sensing.

Citation:

J. J. Konkle, P. W. Goodwill, D. W. Hensley, R. D. Orendorff, M. Lustig, S. M. Conolly, "Magnetic Particle Imaging X-space Reconstruction using Convex Optimization.," In Preparation, title may change.

Chapter 2

Development of a FFL for Projection MPI

2.1 Introduction

X-ray and CT angiography are critical tools that help cardiologists diagnose and treat stroke and vascular diseases. There are nearly 80M iodinated angiograms each year in the USA [33]. Combined risks of X-ray and CT angiography include: catheterized injection trauma, ionizing radiation for both patient and medical personnel, and also contrast induced nephropathy (CIN) [53],which is especially worrisome for Chronic Kidney Disease (CKD) patients. Here we develop MPI with angiography-capability in mind. MPI has the potential to remove all three of these risks to patient and medical personnel.

Current fluoroscopy techniques are capable of imaging at 15 to 30 frames per second (FPS). We must increase the scanning speed of MPI if it is to compete with existing modalities and gain adoption by healthcare professionals. Current MPI scanners have been demonstrated to scan at 47 FPS for imaging volumes of 2.04 cm x 1.2 cm x 1.68 cm [77]; however, high resolution 3D scans over larger volumes will push the limits of scanning speed due imaging constraints such as patient heating and magnetostimulation.

In this chapter, we present the development of a Field Free Line magnet, which will enable MPI projection imaging. An FFL is an entire line in space with zero magnetic field magnitude, and the entire line contributes to the MPI signal instead of just a single point. Therefore, we can create a projection image from an FFL. This will increase scanning speed by a factor of 128 in a standard imaging volume of 128^3 voxels.

Using an FFL with CT reconstruction techniques in a simulation study, Weizenecker et al. demonstrated an 11 fold increase in SNR over existing 3D scan techniques [76]. Knopp et al. then calculated that a FFL can be generated using a minimum of three coil pairs in a $sin(2\varphi)$ current pattern, though four coil pairs were shown to have best efficiency while still allowing rotation of the FFL [38]. Power efficiency was then improved to 1.4 times existing field free point 3D scanners with the use of a new current loop configuration containing one

static gradient pair [34]. Also, a static FFL, one that does not rotate, has been simulated using only two coil pairs [35].
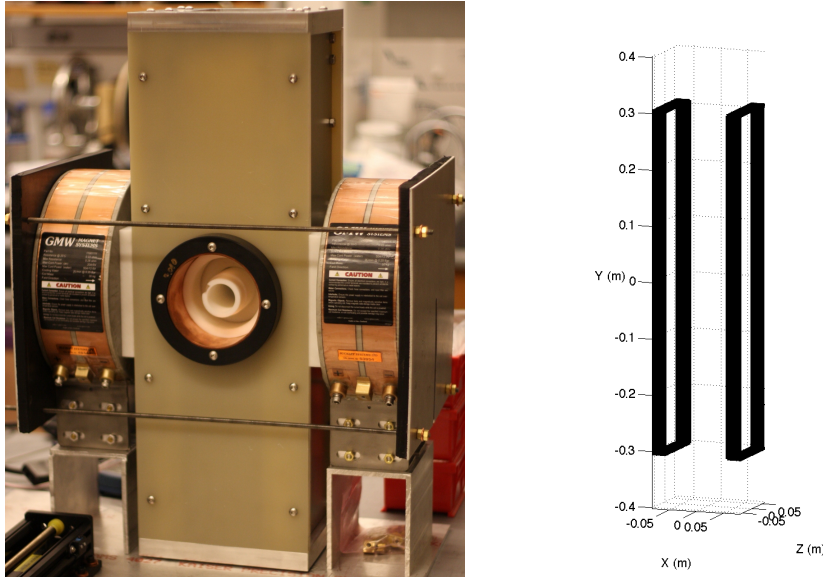
Figure 2.1: FFL Gradient Magnet. (a) Photo of our 2.25 T/m FFL permanent magnet gradient with a 3.5 cm (1.38 in) free bore (b) Simulation framework for our permanent magnet showing magnet dimensions, which correspond to coils used in the surface current model explained in section 4. The photo and simulation framework are roughly aligned to the same coordinate frame to illustrate the permanent magnet orientation. Future FFL magnets have the potential to increase MPI scan rate or increase SNR.

To date, no physical FFL MPI scanner has been constructed and no experimental results have been published from an MPI-capable FFL magnet. In section 2 of this chapter, we show the permanent FFL magnet we have designed and built, and in section 3 we explain how this magnet was assembled. In section 4 we illustrate the design and simulation techniques used. In section 5 we show experimental measures of the magnetic field produced by our FFL magnet, and we present a comparison between actual and simulated magnetic fields. We then illustrate the quality of the FFL achieved.

2.2 Hardware

We have developed and built the FFL magnet shown in Figure 2.1. The design uses a two segment Halbach quadrupole to obtain a 2.25 T/m FFL gradient. The outline of the two gradient-producing magnet segments are shown in figure 2.1. The magnet segment dimensions are 2.5 cm (1 in) thick along the X axis, 61.0 cm (24 in) tall along the Y axis, 12.7 cm (5 in) wide along the Z axis, and have 11.4 cm (4.5 in) spacing along the X axis.
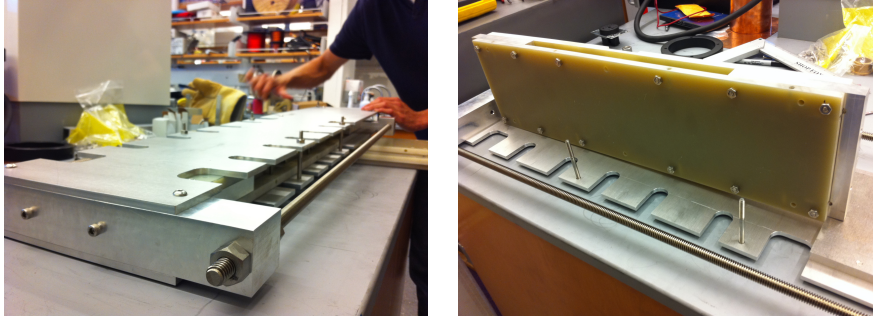
Figure 2.2: Hardware Assembly. Six magnet sections are assembled into each of the two Halbach quadrupole segments. The assembly jig was needed to create the force necessary to align the six permanent magnet sections side-by-side.
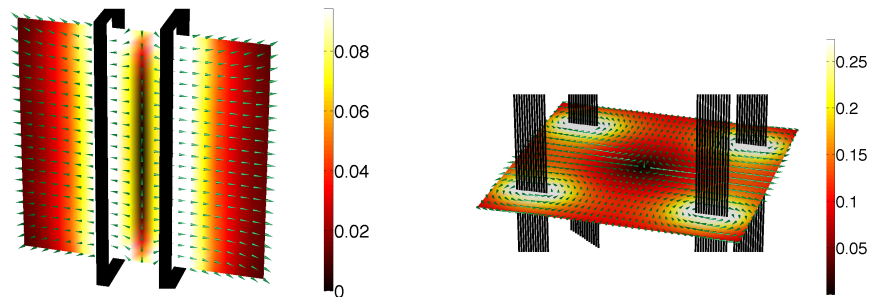
Figure 2.3: Magnetic Field Magnitude Plots. (a) Simulation of the magnetic field along the Z=0 plane. (b) Simulation of the magnetic fields along the Y=0 plane. Both plots show the magnetic field produced by our FFL permanent magnet segments using the current law. Coils around the outer diameter accurately simulate the magnetic field of the permanent magnets using the Biot-Savart Law. Our simulations show that we can create a homogeneous FFL across the FOV using two permanent magnets.

2.3 Assembly

The two FFL gradient segments were constructed from six permanent magnet sections. Each NdFeB permanent magnet section is of size 2.5 cm (1 in) thick along the X axis, 10.2 cm (4 in) tall along the Y axis, and 12.7 cm (5 in) wide along the Z axis. When aligned adjacent to each other along the Y axis, these magnets oppose each other with a large force. To assemble each segment, a custom jig was manufactured as shown in figure 2.1. The magnet sections were slowly cranked together and bolted in place using the jig. One of the two halves of the magnet assembly is shown positioned on top of the assembly jig in figure 2.1.

2.4 Design and Simulation

We created a custom tool to design the FFL magnet. A Biot-Savart solver was written in Matlab (Mathworks - Natick, Massachusetts) to calculate the magnetic fields from an arbitrary current loop. Using the surface current model, magnetic fields from a permanent magnet can be simulated using current loops [16]. A current loop with the proper current wrapped around the outer diameter dimensions of the desired permanent magnet produces the required magnetic field according to $j_m = M \times \hat{n}$, where j_m is the surface current density, M is the magnetization, and $\hat{n}$ is the surface normal. Figure 2.1 shows the current loops used to simulate our design, and figure 2.3 shows the resulting magnetic fields. We assumed the relative permeability, μ_r, of NdFeB was 1.00, while the actual relative permeability is 1.05. Thus, the simulated magnetic fields are at least 95% accurate.

The FFL permanent magnet segments were designed with bore size, gradient magnitude, access, and gradient uniformity in mind. To allow access to the imaging bore, a two segment Halbach quadrupole was chosen though a greater number segments would produce a larger gradient. For a constant magnet type and configuration, there is a trade-off between bore size and gradient magnitude. The X and Z axis dimensions and spacing of the permanent magnets were chosen to create a gradient that is equal in both dimensions. The Y dimensions were chosen to keep the FFL uniformly zero across the field of view.

2.5 Methods and Results

Figure 2.4 shows the measured and simulated magnetic field magnitude of the FFL magnet. A set of X, Y, and Z axis stages were used to position LakeShore HMNA-1904-VR and HMNT-4E04-VR Hall Probes to measure magnetic field components with a LakeShore 475 DSP Gaussmeter. The magnetic field magnitude was then calculated from each field
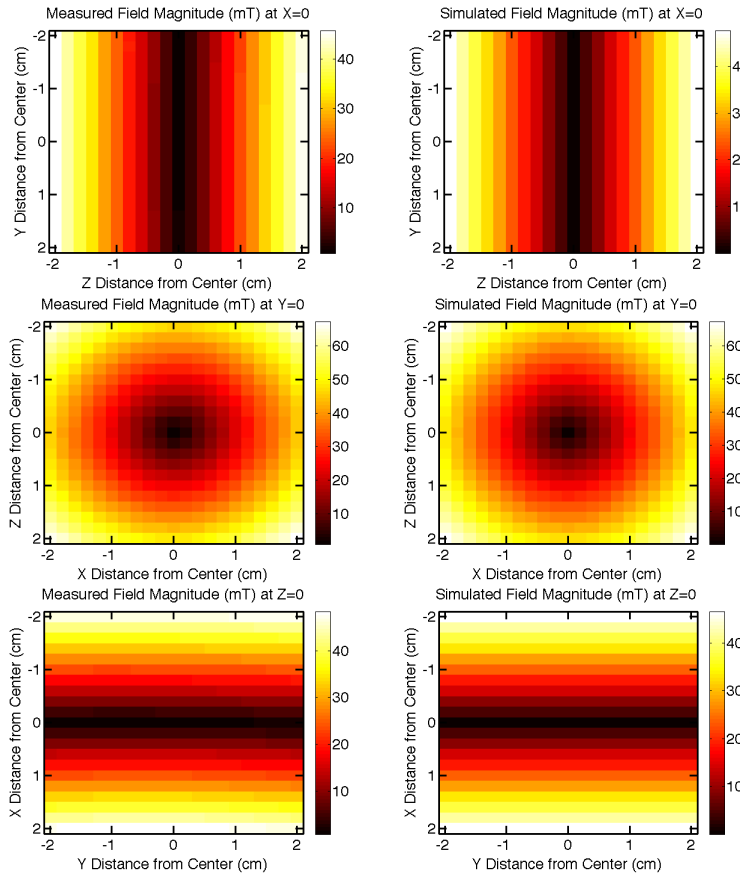
Figure 2.4: Measured vs. Simulated Magnetic Field Plots. Excellent agreement is shown between simulated and measured magnetic fields. Over the entire 4 x 4 x 4 cm^3 field of view, the maximum deviation of simulated to measured fields is 3.7 mT, and the RMS deviation is 1.4 mT.
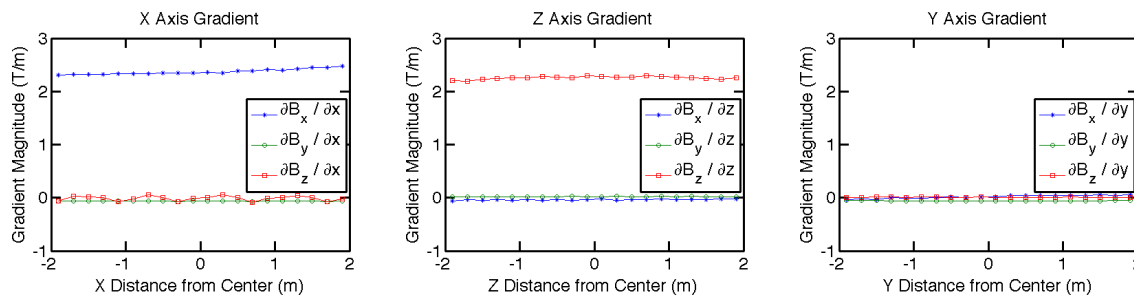
Figure 2.5: Experimentally Measured Gradient Components Along Each FFL Axis. Note that the gradient is homogeneous at approximately 2.25 T/m along both the X and Z axes. Note that the field is close to zero - within 2 mT - along the entire length of the FFL (Y axis). This is the first experimental demonstration of an MPI imaging-capable FFL gradient.

component. The maximum deviation of simulated to measured magnetic fields is 3.7 mT within the 4 x 4 x 4 cm^3 field of view (FOV). The maximum root mean square deviation of measured versus simulated field magnitude is 1.4 mT. The overall maximum magnitude of the magnetic field in the FOV is 67.3 mT.

Figure 2.5 shows the gradient components along each axis of the FFL Magnet. The gradient is homogeneous at approximately 2.25 T/m along both the X and Z axes with a maximum deviation of 3.4% along the gradient. The field is homogeneous at 0 mT along length of the FFL (Y axis) with a maximum magnitude of 2.0 mT.

2.6 Discussion

This chapter shows the first experimental demonstration of a FFL magnet designed for mice imaging. We have illustrated the design, construction, simulation, and testing of a 2-segment Halbach quadrupole magnet configuration [27], which was chosen based on its excellent symmetry. It produces a highly homogeneous magnetic field gradient along the FFL. The quadrupole magnet produces zero field along the entire field free line while the field normal to the FFL does not degrade. In future work, we plan to produce an x-space MPI projection image from the FFL magnet. We also plan to use optimization techniques to improve FFL designs as well as the image quality, imaging speed, and power consumption in MPI imaging.

Chapter 3

Projection Reconstruction MPI

3.1 Introduction

The previous chapter described the design and construction of a Field Free Line (FFL), which localizes USPIOs along a line. Rapidly scanning this line in space creates a projection image of the particle concentration [25]. By reducing image dimensionality from 3D to 2D, projection MPI improves speed by two orders of magnitude over imaging using a FFP. This speed improvement can be traded for signal-to-noise ratio (SNR) via averaging. In previous work, we demonstrated experimental images from a projection MPI scanner [25]. We described the x-space theory of an FFL, found the analytical point spread function of an x-space FFL scanner, and determined FFL homogeneity requirements [25].

A projection imaging format, coupled with sample or scanner rotation, can be used to acquire data necessary to reconstruct a 3D image volume, as is done in computed tomography (CT). Fig. 3.1 illustrates the acquisition of a single projection, $g(\ell, \theta)$, at a single rotation angle, θ. Multiple projections can be acquired by varying θ. Filtered backprojection (FBP), a projection reconstruction algorithm, is commonly used to reconstruct an image. As the name suggests, filtered backprojection first filters the projections using a ramp filter and subsequently projects (or smears) the filtered projections across the resulting image space at the angle of acquisition [59]. The multiple back-projected images are summed to reconstruct the output image. The step of adding multiple projections together increases SNR, a primary benefit of projection reconstruction. For the same acquisition time as a 3D scan with a FFP, projection reconstruction MPI (PR MPI) has the potential to increase SNR by an order of magnitude due to signal averaging. This sensitivity gain would be useful to detect smaller concentrations of USPIO tracer.

First introduced to the MPI field in 2008 [76], early FFL studies employed simulation and theory to demonstrate the SNR gain of projection reconstruction MPI. A simulation study introduced an electronically rotated and shifted FFL design, where a system matrix inversion with regularization was used to reconstruct images. This simulation showed SNR gains of the FFL over a traditional FFP acquisition [76]. Followup studies included designs
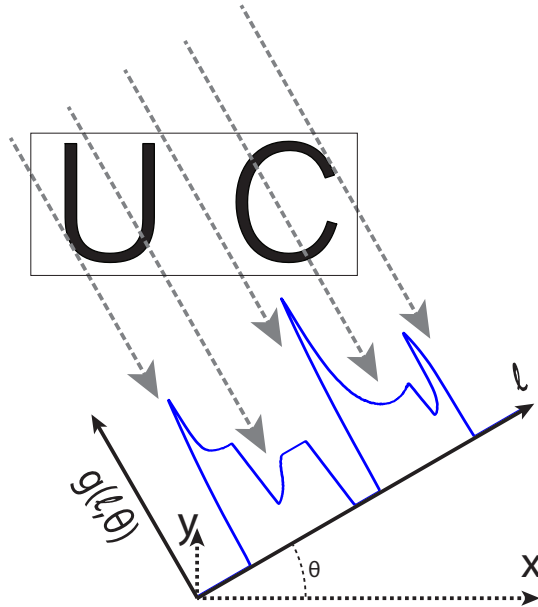
Figure 3.1: Diagram of projection reconstruction imaging. The Field Free Line magnetic field is rotated at an angle θ followed by the acquisition of a single projection, $g(l, \theta)$. Multiple projections are acquired by varying θ, and a projection reconstruction algorithm is used to reconstruct a 3D image. A single rotation angle of a projection reconstruction imaging sequence is shown. Here, a rotated projection is shown for clarity while sample rotation is used in our imaging system (see Fig. 3.2).

to simplify and reduce power consumption of the initial FFL design and experimentally demostrated a shifted and rotated FFL [38, 34, 12]. An alternative FFL design with two Maxwell coil pairs has been introduced to reduce MPI system complexity [35]. Additionally, a study related projection reconstruction in MPI to the Fourier slice theorem and illustrated image reconstruction with two receive coils and an electronically rotated FFL [37].

In this chapter, we present the first experimental demonstration of PR MPI. We adapt x-space theory to projection reconstruction MPI, including the derivation of the theoretical PSF, resolution, SNR, and number of projections required. We augment our FFL projection MPI system with sample rotation to produce a projection reconstruction MPI system. Scanning methods using sample rotation, similar to this system, are common in MicroCT scanners [32, 29]. We then present projection reconstruction 3D volumes of the PSF, imaging phantoms, and post-mortem mice. This is the first experimental validation for projection reconstruction MPI techniques, which will enable higher SNR for detecting USPIO particles *in vivo*.
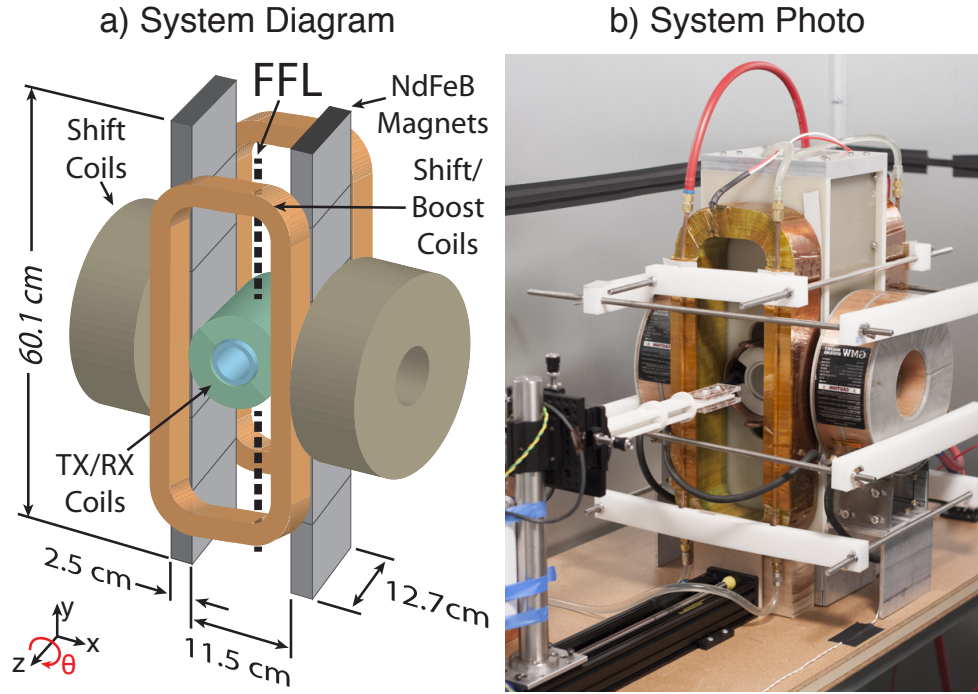
Figure 3.2: The Berkeley Projection Reconstruction MPI System. a) Diagram of the system magnets including a 2.4 T/m NdFeB gradient, and inductive shift, boost, transmit and receive coils. b) System photo additionally showing the sample holder, which includes a motor-driven rotary table that enables sample rotation.

3.2   Theory

In this section, we describe the theory of projection reconstruction in x-space MPI. As seen in our PR MPI system in Fig. 3.2, we use the convention that the FFL is oriented along the y axis, the drive field excitation vector is along the z axis, and the slow focus or shift vector is along the x axis. We assume the particle response is instantaneous and has no relaxation effects.

To acquire multiple projection images necessary for projection reconstruction, we rotate the sample around the z axis, which is equivalent to FFL magnetic field rotation around the z axis for a system with excitation coils and receive coils oriented along the z axis. The instrument frame, $[x \ y \ z]^T$, is the non-rotated frame, while the sample frame, $[x' \ y' \ z']^T$, is the rotated frame. The magnetic field of the FFL oriented along the y axis can be described using a gradient matrix $\mathbf{H}(\mathbf{x}) = \mathbf{G}\mathbf{x}$. This field is translated along the x axis using a homogeneous focus or shift field, $\mathbf{H}_s = H_x\hat{\mathbf{i}}$. The particles are excited along the z axis by a homogeneous field, $\mathbf{H}_e = H_z\hat{\mathbf{k}}$, as illustrated in Fig. 3.3. The combined magnetic field becomes
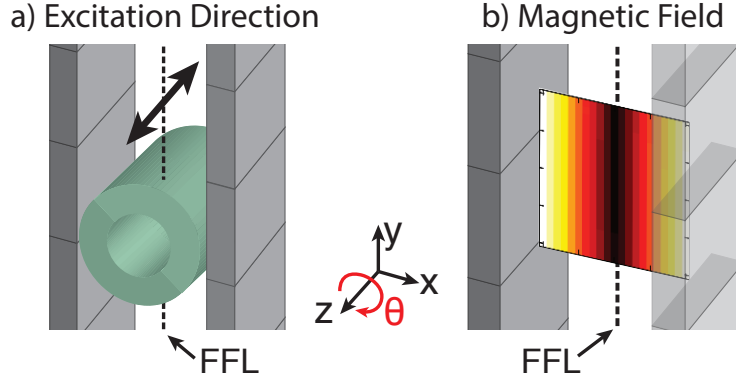
Figure 3.3: FFL excitation diagram and magnetic field plot. (a) Diagram of the permanent magnets that generate the FFL and of the solenoidal transmit coil that excites USPIOs at 20 kHz. The arrow above the transmit coil indicates that the excitation direction is along the z axis. The ~2 Hz slow shift of the projection occurs along the x axis. (b) Magnetic field plot of the FFL with darker colors corresponding to smaller field strengths.

$$\mathbf{H}(\mathbf{x}) = \mathbf{Gx} + H_x\hat{\mathbf{i}} + H_z\hat{\mathbf{k}}$$

$$= \begin{bmatrix} G_{xx} & 0 & 0 \\ 0 & 0 & 0 \\ 0 & 0 & G_{zz} \end{bmatrix} \begin{bmatrix} x \\ y \\ z \end{bmatrix} + \begin{bmatrix} H_x \\ 0 \\ H_z \end{bmatrix}, \tag{3.1}$$

where $\mathbf{x}$ [m] is the position vector in the instrument coordinate system and $\mu_0 G_{ab}$ [T/m] is the partial derivative of the magnetic field in the a direction with respect to b [25, 37]. $\mu_0 G_{ab}$ is also known as the gradient strength of the system. $\mu_0 = 4\pi \times 10^{-7}$ T $\cdot$ m/A is the permeability of free space. $G_{xx} = -G_{zz}$ as required by Maxwell's equations.

In Appendix A.1, we derive the magnetic field of the shifted and rotated FFL. To determine where the FFL lies in space, we calculate the magnitude of the magnetic field (which is squared to simplify the result here),

$$|\mathbf{H}'(\mathbf{x}', \theta)|^2 = (G_{zz}z' + H_z)^2 + G_{zz}^2(x'\cos\theta + y'\sin\theta - H_x/G_{zz})^2, \tag{3.2}$$

where θ [rad] is the angle of rotation. By inspection, we see that the field is zero when

$$z' = -H_z/G_{zz} \tag{3.3}$$

and

$$x'\cos\theta + y'\sin\theta = H_x/G_{zz}. \tag{3.4}$$

We define

$$\ell = H_x/G_{zz}. \tag{3.5}$$

Thus, the FFL lies on

$$x' \cos\theta + y' \sin\theta = \ell \tag{3.6}$$

at a z position defined by the H_z excitation field and the gradient. Note that physically ℓ [m] represents the shift position perpendicular to the FFL. This is the standard notation used in CT [59]. The USPIO signal is integrated along this line, allowing a projection image of the sample to be acquired at any rotation angle as illustrated in Fig. 3.1. The variables H_x, H_z, and θ give us precisely the control we require to collect a complete set of projection data.

After acquiring projections, a 3D volume can be created using PR methods such as the direct Fourier method, convolution backprojection, FBP, or other statistical, iterative, and optimization approaches [5, 63, 70, 59, 78]. In this work, we used filtered backprojection due to its simplicity and robustness. The FBP algorithm first filters the acquired projections with a ramp filter in the spatial frequency domain and then backprojects the filtered projections. This operation essentially smears the filtered projections across the reconstructed image at the angle of incidence. The backprojected images are added to create a 3D volumetric image.

To derive the PSF for projection reconstruction MPI, we can start from the PSF for a single projection, $\mathbf{h(x)}$ [25]. The PSF after PR can then be calculated using the inverse Abel transform [6], which is equivalent to the Fourier transform followed by the inverse Hankel transform,

$$h_{pr}(r) = \mathcal{A}^{-1}\{h\} = \mathcal{H}^{-1}\left\{\mathcal{F}\{h\}\right\}, \tag{3.7}$$

where $\mathcal{A}^{-1}$ is the inverse Abel transform operator, $\mathcal{H}^{-1}$ is the inverse Hankel transform operator, and $\mathcal{F}$ is the forward Fourier transform operator. There is no closed-form expression for the Fourier transform of the MPI PSF along the x axis, but fortunately, it is well approximated (<1 % RMS full-scale error as calculated by Equation A.7) by a Lorentzian. The result is a closed form approximation of the PR PSF in the xy plane,

$$\hat{h}_{pr}(r) = \sum_{k=1}^{2} \beta_k \left(\alpha_k^2 + r^2\right)^{-3/2}, \tag{3.8}$$

where r [m] is the distance along the radial axis. α_1, α_2, β_1, and β_2 are fitted constants determined in Appendix A.2. Equation (3.8) is accurate within a 2.4% RMS full scale error (calculated with Equation A.7) when compared across a 6 cm FOV to the theoretical PSF, which can be computed via filtered backprojection on the 1D projection PSF. This approximation allows us to determine how system and particle parameters affect resolution and the number of projections required in PR MPI. A detailed derivation of this approximation is included in Appendix A.2.

We use the approximate PSF in Equation (3.8) to determine the resolution of a PR MPI system. The resolution according to the Houston criterion [30], or full width at half maximum (FWHM), of Equation (3.8) is

$$FWHM_{PR} \approx \frac{34 k_b T}{\mu_0 G_{xx} \pi M_{sat} d^3},$$
(3.9)

where $\mu_0 M_{sat} \sim 0.6$ T is the saturation magnetization, d $[m]$ is the particle diameter, $k_b = 1.38 \times 10^{-23}$ $m^2 \cdot T \cdot A \cdot K^{-1}$ is Boltzmann's constant, and T [K] is the temperature. Note that the FWHM resolution before PR also has the same form; however, PR imaging improves resolution by approximately 40% along the x axis. The resolution scales inversely with the gradient and the cube of the particle diameter. In a system with a 2.4 T/m gradient and with particles that can be modeled as theoretical particles of 22.7 nm in diameter (see Section 3.3), we would expect a FWHM of 3.3 mm in the xy plane.

We also use the PSF of Equation (3.8) to determine the minimum number of evenly-spaced projections between 0 and 180 required to avoid aliasing in a PR image. As discussed in Appendix A.3, we can use the following formula as guidance [5],

$$N_{proj} > \pi \cdot FOV_{xy} \cdot K_{max},$$
(3.10)

where FOV_{xy} [m] is the maximum field of view (FOV) of x and y and is set by the system user. K_{max} [m^{-1}] is the largest spatial frequency in the system, which is determined from the system point spread function (PSF). In a system with a 2.4 T/m gradient and with particles modeled as 22.7 nm in diameter (see Section 3.3), $K_{max} \approx \frac{1}{2FWHM} = 0.15$ mm^{-1}. With a $FOV_{xy} = 6$ cm, 28 projections are necessary to avoid aliasing.

The number of projections acquired also affects signal to noise ratio (SNR) of the resulting image. In general, SNR increases by the square root of the number of averages acquired in a system, assuming that the noise is independent and identically distributed. In projection reconstruction, this means that SNR improves $\propto \sqrt{N}$, where N is the number of projections acquired. In practice, if we increase the number of projections from 25 to 100, we will double our SNR as well as decrease aliasing artifacts.

3.3 Methods

Imaging System Construction

A diagram and photo of our imaging system are shown in Fig. 3.2. This system is described in more detail in [25]. We used two NdFeB permanent magnet sections to produce the FFL. Each section was created with six NdFeB permanent magnets assembled with matching magnetization orientation. The two sections were then assembled with opposing magnetization orientation to produce a FFL. This configuration produced a $\mu_0 G_{zz} = -\mu_0 G_{xx} = 2.4$ T/m magnetic field gradient along both the x and z axes with the FFL oriented along the y axis.
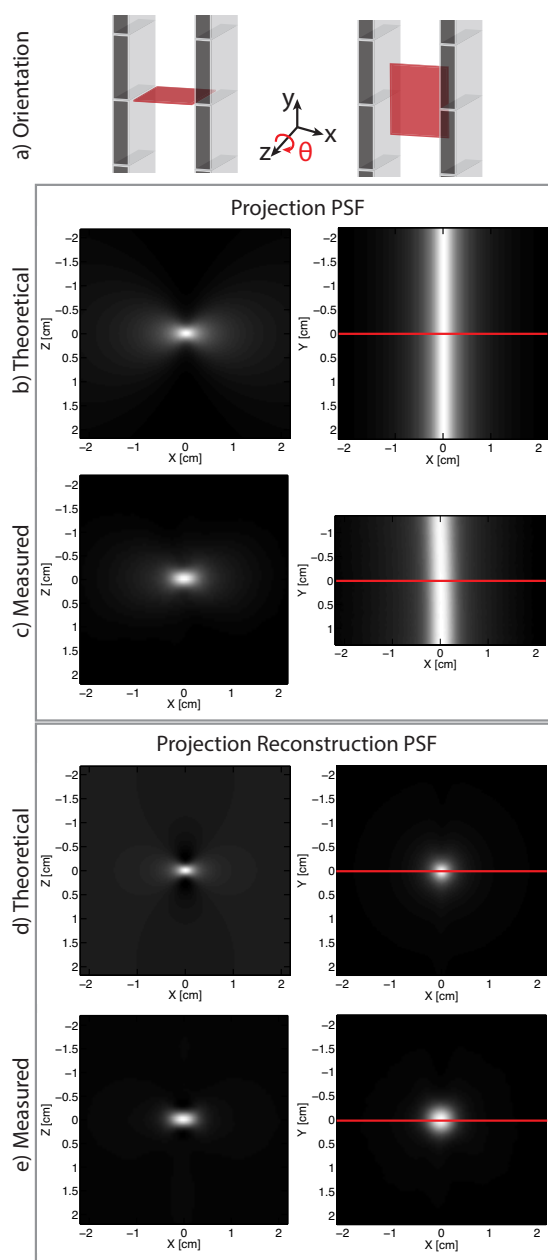
Figure 3.4: Projection PSF and Projection Reconstruction PSFs using filtered backprojection. Cross-section along the red lines are shown in Fig. 3.5. (row a) Diagram indicating the orientation of the plots in the same column below. (row b) Theoretical PSF using Equation (A.4). (row c) Measured projection PSF. (row d) Theoretical projection reconstruction PSF obtained using filtered backprojection on row b. (row e) Measured projection reconstruction PSF. Acquisition time for each projection image was 16 s per image, the XZ FOV was 6 cm × 5.6 cm and 180 projections were acquired.
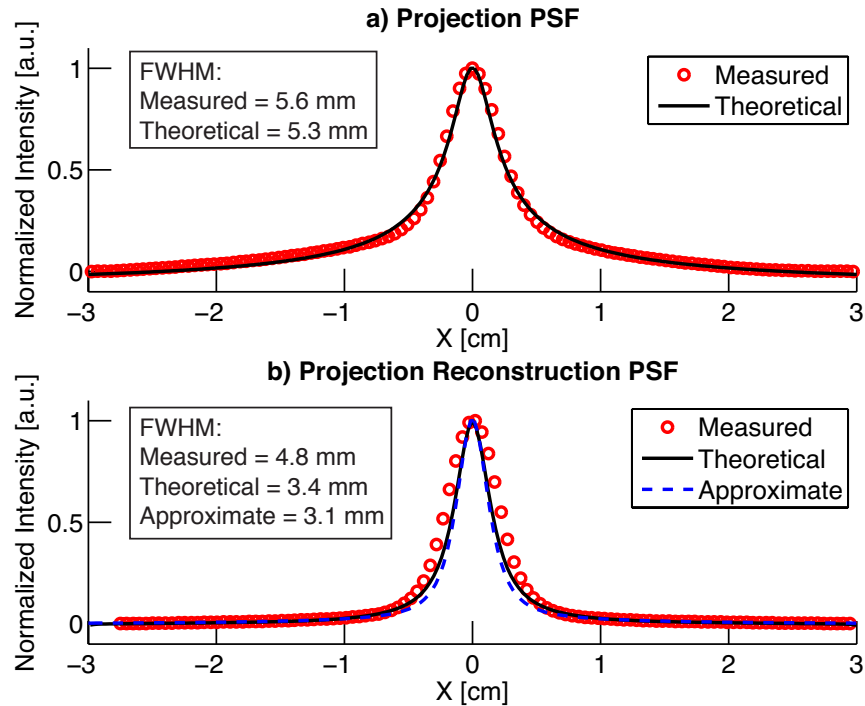
Figure 3.5: Projection PSF and Projection Reconstruction PSF cross-sections from Fig. 3.4. a) Measured and theoretical projection PSFs. Theoretical PSF calculated using Equation (A.4). b) Measured, theoretical, and approximate Projection Reconstruction PSFs. The approximate PSF was obtained using Equation (3.8), while the theoretical PSF was obtained via filtered backprojection on Equation (A.4).

We attached two electromagnets (GMW 11901111, San Carlos, CA) to shift the FFL in the x direction and two custom electromagnets to shift the FFL in the z direction. Switching amplifiers (Copley Controls 234) drove these coils with a maximum 350 A peak current, which produced a x direction FOV of 6 cm. A linear amplifier (AE Techron LVC5050) drove a resonant transmit coil, which created the 20 kHz drive field oriented in the z direction. The receive chain consisted of an inductive receive coil, a notch filter at the fundamental drive frequency, and low noise preamplifiers (SR560 and SIM911). Custom software (Mathworks Matlab, Natick, MA) controlled a data acquisition card (NI PCIe-6363, Austin, TX), which drove the amplifiers and digitized the signal. A one axis translation stage (Velmex, Bloomfield, NY) was used to increase the FOV to a maximum of 22 cm in the z direction using a moving table scan.

Image Acquisition & Projection Reconstruction

To obtain an MPI tomographic 3D volume, we employed FBP after acquiring projection images at multiple angles. A motor driven rotary table (Velmex, Bloomfield, NY) rotated

the sample to allow the acquisition of images at linearly spaced angles from 0 degrees to 180 degrees. Procedurally, the scanner obtained a projection image at one rotation angle, rotated the sample, and then acquired another projection image (see Fig. 3.6c). After acquiring all images, the FBP algorithm was employed. The algorithm selected a 1D slice parallel to the x axis in each image at corresponding z locations and then filtered each slice using a ramp filter in the spatial frequency domain to compensate for denser sampling at the center of k-space [59, 63]. After filtering, the slices were backprojected at the acquisition angle, and a 3D volume was reconstructed. Projection scans were taken twice, once in the forward translation z direction and once in the reverse direction, and were averaged to form the final image.
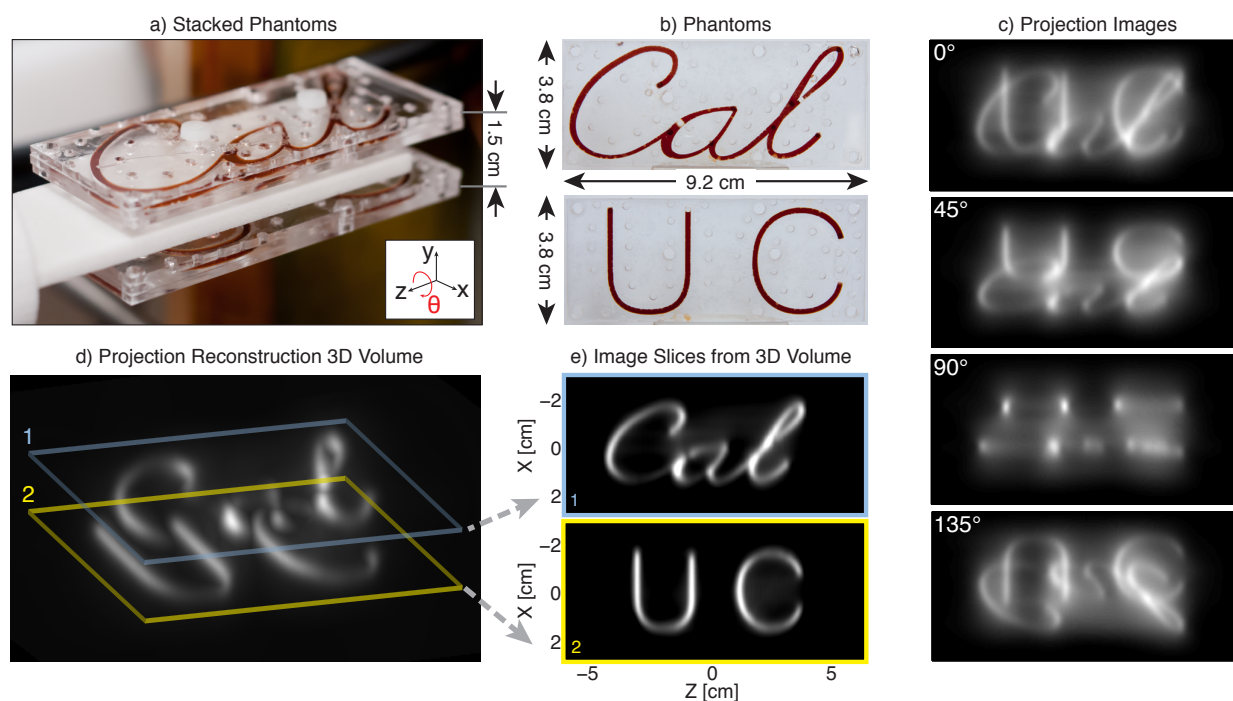
Figure 3.6: Undeconvolved Filtered Backprojection MPI Experimental Images. a) Acrylic phantoms stacked in preparation for imaging. b) Photos of phantoms with 50 mM Resovist (10x diluted). c) Four of 180 acquired projection images with rotation angle, θ, denoted on each image. d) Maximum intensity projection of the 3D volume reconstructed using filtered backprojection on the 180 projection images. e) Two slices of the 3D imaging volume at the plane of each imaging phantom with slice thickness of 0.5 mm. Each projection image acquisition took 39s for a total imaging time of 117 min with N=2 averages (N=1, 59 min) with a 6 cm by 12 cm FOV.

After reconstructing a 3D image volume, the software exported the entire volume in DICOM file format. The DICOM files were imported to Osirix (Pixmeo, Switzerland), where maximum intensity projection and volume rendered images were created.

PSF Measurement and Comparison

To measure the PSF of our imaging system, we imaged a 3.5 μL vial of undiluted 0.5 M Resovist (Schering AG, Germany), a USPIO tracer for MRI. The Resovist vial contained the sample within 3 mm^3, which was smaller than the resolution of our imaging system and could be considered a point source. The scanner acquired 180 projection images, each with an acquisition time of 16 s and a FOV of 6 cm by 5.6 cm. A 3D volume was then reconstructed as described in Section 3.3.

   Projection PSF calculations were performed using Equation (A.4) and approximate PR PSFs were calculated using Equation (3.8). For theoretical PR PSFs, we used Equation (A.4) and applied filtered backprojection. Parameters were chosen to match our imaging system: $\mu_0 G_{zz} = -\mu_0 G_{xx} = 2.4$ T/m and $T = 300$ K. The particle diameter of Resovist has been been reported as many different diameters [25, 60]. To determine the effective Resovist diameter in our sample, we fitted the theoretical projection PSF of Equation (A.4) to the measured projection PSF with the particle diameter as the free parameter. This fit resulted in a diameter $d = 22.7$ nm. This diameter was used for all calculations. Since the DC information is not available in MPI data [25, 47, 45], we restored the DC value by assuming the MPI signal at the boundaries of the image was zero.
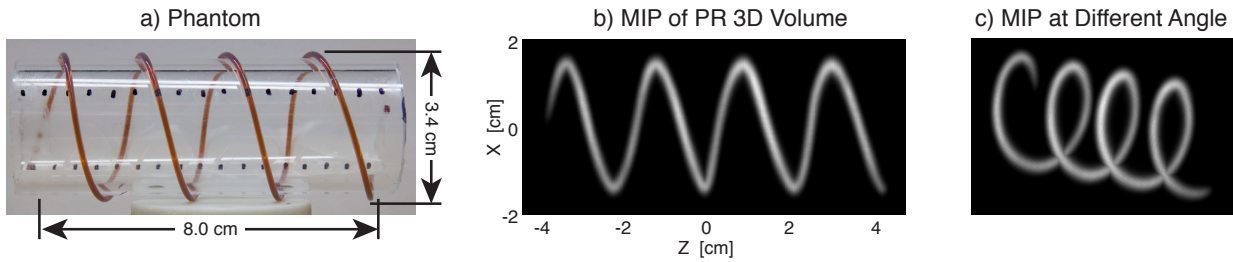
Figure 3.7: Phantom Imaging. a) Photo of a helical imaging phantom. Tubing with ID 0.8 mm (OD 1.4 mm) was filled with 50 mM Resovist (10x diluted). b) Maximum intensity projection (MIP) image with no deconvolution taken in our Projection Reconstruction MPI scanner. c) MIP at a different angle to illustrate the 3D volume. A total of 60 projection images were acquired with a time of 39s each and a 6 cm by 12 cm FOV. The total imaging time was 39 min.

Phantom Experiments

To test the performance of our Projection Reconstruction MPI system, we created custom acrylic phantoms with Resovist tracer. The phantoms were composed of three laser cut sheets of acrylic with the middle layer containing the desired Resovist distribution pattern. Fig. 3.6a shows images of two acrylic phantoms stacked to create a 3D Resovist distribution. Phantom imaging was performed with 180 projection images, a 6 cm by 12 cm FOV, and

an acquisition time of 39 s per projection. The total acquisition time was 2 h. Filtered backprojection was used to create a 3D volume as described in Section 3.3.

A helical imaging phantom (pictured in Fig. 3.7a) was created using cylindrical piece of acrylic with a 3.4 cm outer diameter. Tubing with ID 0.8 mm (OD 1.4) was wrapped around the acrylic and was filled with 50 mM Resovist (10x diluted). Sixty projections, each with a 6 cm by 12 cm FOV and 39 s scan time were taken. The entire volume was acquired in 39 min.

Mouse Imaging

We prepared a mouse for imaging by injecting 100 µL of undiluted Resovist into the tail vein and sacrificing after 30 s. The mouse was then imaged in the PR MPI system with 180 projections, each with a FOV of 6 cm by 12 cm along the x and z axes respectively. Each projection image took 3 min to acquire for a total imaging time of 540 min. After acquisition and reconstruction using FBP, we applied deconvolution with Wiener filtering [19] using the theoretical PSF. The small amount of deconvolution sharpens the image by reducing the effect of the long tails of the PSF.

3.4 Results

In Fig. 3.4, we compare the theoretical PSF with a PSF measured from our imaging system. Images in the left column show the xz plane while images in the right column show the xy plane. The top set of four boxed images compares projection format PSFs while the bottom set compares projection reconstruction format PSFs. Note the close agreement between theoretical and measured PSFs.

Fig. 3.5 compares image cross-sections of measured, theoretical, and approximate PSFs in both projection and projection reconstruction formats. Fig. 3.5a plots a cross-section of the measured and theoretical projection PSFs in Fig. 3.4b and 3.4c, demonstrating agreement between the two. Fig. 3.5b plots cross-sections from the measured and theoretical projection reconstruction PSF from Fig. 3.4d and 3.4e. Fig. 3.5b also plots an approximate projection reconstruction PSF, calculated from Equation (3.8). For comparison, the FWHM is listed for each plot. Note the slight decrease in FWHM in the PR results over the projection results as predicted in Section 3.2. Also note the close match in theoretical, approximate, and measured plots and FWHM values.

Fig. 3.6c shows four of the 180 projections acquired at multiple angles of rotation around the theta axis for our stacked acrylic imaging phantom. A maximum intensity projection through the imaging volume is displayed in Fig. 3.6d. Fig. 3.6e shows two slices through the image volume. No deconvolution has been performed in any of the images in Fig. 3.6. Note, we can see two large air bubbles in both the photo of the phantom and the output PR image. This can also be seen but with more difficulty in the projection images. Also, in the projection images of Fig. 3.6c, note the signal summation that occurs along the field free

line, which causes bright points at differing locations along the phantom image depending on rotation angle. These bright points occur at locations where the FFL integrates signal in both acrylic phantoms. While we see these bright spots in the projection images, the PR images fully resolve all features in 3D. The ability to resolve the bubble and the lack of signal summation illustrate the diagnostic quality improvement of 3D PR imaging over projection format imaging.

Fig. 3.7 contains maximum intensity projection images from a helical phantom. Two perspectives are shown of the reconstructed volume. Once again, these images illustrate the capability for very high SNR with PR MPI.

Fig. 3.8 shows a projection reconstruction image of a post-mortem mouse injected with Resovist. The tracer accumulation can be seen in the heart, liver, and brain.
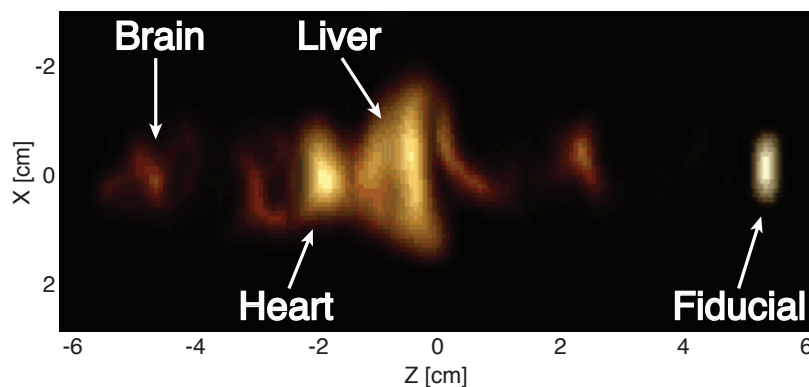
Figure 3.8: PR MPI image of a mouse injected with 100 uL of 0.5 M Resovist into the tail vein and sacrificed after 30 s. The tracer accumulation appears in the heart, liver, and brain. 180 projection images were taken, each with a 6 cm by 12 cm FOV and 3 min acquisition time.

3.5   Discussion

Here, we have demonstrated the first experimental implementation of filtered back projection 3D MPI scanning. The same projection reconstruction MPI scanner could be used in a 2D projection format to produce real-time images or with averaging to produce high SNR 2D images. The flexibility enabled by FFL imaging for high speed or high SNR 2D imaging, as well as high SNR 3D images, could be extremely useful in the clinic. This relationship could be similar to the relationship that currently exists between X-ray and CT. Applications such as angiography demand a high speed format to faithfully capture the range of cardiac motion so X-ray fluoroscopy is often used. Patients would benefit from projection MPI that utilizes no ionizing radiation and tracers that are completely safe, especially for CKD patients [48].

For applications not requiring high speed but benefitting from a high SNR 3D image, CT is used. In MPI, possible applications of this format include cancer and stem cell imaging.

This chapter presents the first experimental proof that the homogeneity of a real-world, inexpensive permanent magnet FFL can be made adequately uniform (with minimal *fading* [25]) to produce artifact-free FBP reconstructions. This bodes well for future higher strength FFL magnets. In the future, we intend to develop a scaled-up PR MPI system. Such a system could include a 20 T/m superconducting gradient with a 256^3 image grid. A gradient of this strength would have a 400 μm xy plane resolution with Resovist according to Equation (3.9). With a 6 cm FOV, we would need to acquire 235 projections to avoid aliasing according to Equation (3.10). With MPI we have the benefit that additional projections do not cause additional patient radiation dose since no ionizing radiation is involved. Challenges to development of such a system would include higher receiver bandwidth, better FFL magnet homogeneity (to prevent *fading* artifacts [25]), and reconstruction time scale-up.

We also plan to implement a helical moving-bed scan similar to current CT technology. We estimate that we could acquire a full 3D volume in approximately 5 minutes with our current imaging system via this scanning pattern (partial FOV of 8 mm, helical pitch of 4 mm to allow 50% overlap, 10 s per rotation). Alternatively, we could implement z axis focus field coils (unused in this chapter), which would allow 3D volume acquisition in approximately 30 s (partial FOV of 8 mm, z axis shift of 4 cm and helical pitch of 4 cm, 10 s per rotation). Future scanner hardware development could also include other rotation methods such as gantry rotation or electronic FFL rotation.

As an alternative to Nyquist sampling, we could use compressed sensing techniques to reduce the number of projections taken and speed imaging time. In a human sized scanner with a bore of 30 cm and a gradient of 8 T/m (1 mm resolution with Resovist), 470 projections would be required for non-aliased sampling using the Nyquist criteria. Compressed sensing could allow a much smaller number of projections, thus allowing a faster image acquisition for time resolved datasets [49, 9, 71].

It is interesting to compare MPI projection imaging to MRI projection imaging. With MPI, there is absolutely no concern with phase decoherence along the projection line because all the SPIOs are locked in synchrony with the excitation field. This is in sharp contrast to projection MRI, where B0 inhomogeneity is typically inadequate to prevent excessive decoherence, which is called T2* dephasing in MRI.

The approximate and measured PSFs of Fig. 3.5 match well, illustrating the accuracy of the approximation. The improvement in FWHM after FBP occurs due to image sharpening from the ramp filter. The resolution (and SNR) benefit of PR MPI could be used to view smaller arteries in a high resolution 3D PR MPI as opposed to 3D scan with a FFP.

Equation (3.10) suggests that we only need 28 instead of 180 projections to obtain a non-aliased PR MPI image with our system. Here, we have used more projections to demonstrate artifact free and high SNR images. SNR is extremely high even in our university prototype. This bodes well for the future sensitivity of a professionally engineered system.

3.6 Conclusion

In this chapter, we presented the world's first experimental projection reconstruction MPI system. A permanent magnet FFL was shown to be buildable to the tolerance required for artifact-free FBP. We designed, built, and debugged the associated PR MPI subsystems such as the drive field generation, focus field generation, receive channels, sample rotation, and image acquisition. The approximate PR PSF was derived and shown to correspond accurately to data. The theoretical FWHM, number of projections required, and the SNR gain in projection reconstruction MPI were derived as well. We demonstrated that FBP in MPI is experimentally feasible and illustrated the SNR and resolution improvement with PR. We then demonstrated that MPI is capable of producing three dimensional imaging volumes in both phantoms and post-mortem mice. This is promising for the future of PR MPI.

Chapter 4

Twenty-Fold Acceleration of 3D PR MPI

4.1   Introduction

In the previous chapter, we presented experimental 3D images with a FFL using our first generation projection reconstruction (PR) MPI imager [41, 39]. The relationship between 2D projection imaging and 3D PR imaging with a FFL is analogous to the relationship between X-ray imaging and computed tomography (CT). As described schematically in Figure 4.1, our 3D PR MPI imager acquires "parallel-beam" projection images at various angles while the nanoparticle sample (or equivalently the magnet) is rotated around the z axis. Subsequently, a filtered backprojection algorithm reconstructs 3D images of the nanoparticle distribution. Our first generation 3D PR imager used slow mechanical movement in two dimensions: a z axis translation stage (down the bore) and a motor driven rotary table to allow rotated projections. The mechanical inertia of these stages severely limited the imaging speed of the system. Consequently, the fastest previously reported acquisition of a mouse-sized (6 cm by 12 cm) tomographic image required approximately 39 minutes.

In this chapter, we begin with both theory and experimental evidence that demonstrate advantages of 3D PR for human applications. In short, PR MPI has an order of magnitude signal-to-noise ratio (SNR) boost and is not significantly slower than 3D point scanning when human safety limits are imposed. We then demonstrate rapid PR MPI by implementing hardware changes to our current system and developing a fast PR MPI pulse sequence. The hardware was modified to enable slow movement of the FFL along the z axis by introducing a pair of slow shift (or focus field) electromagnets in addition to the existing translation stage. We also designed and implemented the necessary amplifiers, filters, controllers, and software to drive the z shift coils and reconstruct images using them. To allow faster imaging, we improved the x slow shift electromagnet power matching. The receive coil has been redesigned and fabricated to extend the sensitive region from 7 cm to 10 cm. We then developed a PR MPI pulse sequence to drive the updated hardware. In this modified setup,

the imaging speed is limited by the amplifier output voltage limits and the inductance of the slow field shift electromagnets. With these changes, the system acquires a full 3D image in under 2 minutes, demonstrating a twenty-fold speed improvement over our previous mechanically limited imaging system [39].

4.2   Theory

Signal to Noise Ratio of PR MPI

Table 4.1: MPI Scan Time Comparison

Isotropic Gradient Strength -	Native Image Resolution (Resovist Tracer)	T_{2D} 2D Projection (FFL) or Single Slice (FFP) $(10 \text{ cm})^2$	$T_{3D,ffp}$ 3D Image (FFP) $(10 \text{ cm})^3$	$T_{3D,pr}$ 3D Proj. Recon. Image (FFL) $(10 \text{ cm})^3$
10 T/m	1 mm	3.6 s	260 s	560 s
5 T/m	2 mm	0.89 s	32 s	70 s
2.5 T/m	4 mm	0.22 s	4.0 s	8.8 s
1.25 T/m	8 mm	0.06 s	0.50 s	1.1 s

Best case imaging times (no pFOV overlap) for slow field shift limited imaging using the ICNIRP limits of $S_{\max} = 20$ T/s when imaging the human torso with a drive field amplitude of $B_{th} = 7$ mT (see Appendix A.5), and Resovist tracer. We assume a $(10 \text{ cm})^3$ FOV, which would be a reasonable FOV for imaging the human heart. Note that the SNR of a 3D projection reconstruction image is nearly an order of magnitude better than a 3D image taken using a FFP imager.

It is well known [51, 55] that computed tomography (CT) and magnetic resonance imaging (MRI) typically have a $\sqrt{N}$ SNR advantage over point scanning methods (like ultrasound imaging), where N is the number of projections or the number of frequency space (k-space) samples acquired. 3D MPI with a FFP is fundamentally a point scanning technique, so the SNR of one pixel does not increase with the number of pixels scanned. The concept of a FFL was introduced in MPI to take advantage of an SNR gain created due to averaging when each imaging location is acquired multiple times via a shifted and rotated FFL [76]. While imaging times are similar, the resulting SNR of a 3D PR image is an order of magnitude higher than a 3D FFP image.

The major tradeoff with PR and frequency space (k-space) scanning methods as opposed to point scanning methods is the need to avoid spatial aliasing. In 3D FFP scanning, we can simply scan a subject with no fear of aliasing from outside the selected region. This is not the case with 3D PR since aliasing can appear in the resulting image due to undersampling. Fortunately, it is well known that we can prevent aliasing simply by ensuring that the number

of projections adheres to the Nyquist sampling rate:

$$N > \pi FOV_{\mathrm{x},y} K_{\max}, \tag{4.1}$$

where N is the number of projections, $FOV_{\mathrm{x},y}$ is the maximum FOV in the xy plane, and $K_{\max}$ is the maximum radial spatial frequency of the system [39].

Contrasting a PR MPI system and a 3D FFP system with identical noise characteristics, scan time, resolution, pulse sequence, and selection field gradient strength, the SNR relationship can be described as

$$\frac{\mathrm{SNR}_{PR}}{\mathrm{SNR}_{FFP}} = C\sqrt{N} \tag{4.2}$$

where C depends on the interpolation and filtering used during FBP (see Appendix A.4). We have measured a C of ~0.4 experimentally, and we have seen a C value of 1.1 in theory and simulation. In addition, as we describe next, this SNR improvement comes with a scan time that is in the same order of magnitude as that of a 3D FFP system.

MPI Imaging Time

Intuitively, we note that imaging time for 3D PR imaging and 3D FFP imaging will be equal when the number of projections acquired is equal to the number of slices in the 3D image volume. This is because each slice in 3D FFP MPI and each 2D projection in 3D PR MPI require the same acquisition time assuming planar FFP acquisition trajectories.

More rigorously, we can calculate imaging time for MPI systems based on magnetostimulation limits as discussed in Appendix A.5:

$$T_{2D} \approx \frac{\beta \cdot G_{\mathrm{zz}} FOV_{\mathrm{z}}}{2B_{\mathrm{th}}} \frac{G_{\mathrm{xx}} FOV_{\mathrm{x}}}{S_{\max}}, \tag{4.3}$$

$$T_{3D,ffp} = T_{2D} N_{\mathrm{s}} \approx T_{2D} \frac{\beta G_{\mathrm{yy}} FOV_{\mathrm{y}}}{2B_{\mathrm{th}}}, \tag{4.4}$$

$$T_{3D,pr} = T_{2D} N = \pi T_{2D} \frac{FOV_{\mathrm{x},y}}{2\Delta x}. \tag{4.5}$$

where T_{2D} [s] is the 2D projection or single-slice MPI imaging time, $T_{3D,ffp}$ [s] is the 3D imaging time with a FFP, and $T_{3D,pr}$ [s] is the 3D PR imaging time with a FFL. FOV_{i} [m] is the size of the FOV along axis i, $\mu_0 G_{\mathrm{ab}}$ [T/m] is the partial derivative of the magnetic field in direction a with respect to direction b, B_{th} is the drive field peak amplitude determined by magnetostimulation thresholds [66], $S_{\max} = 20$ T/s is the maximum slew rate as defined by the International Commission on Non-Ionizing Radiation Protection (ICNIRP) [31], Δx [m] is the native (i.e., no deconvolution) full-width-at-half-maximum (FWHM) resolution, and

βis a factor ($>$1) determining the overlap extent of the partial FOVs (pFOVs) required for baseline recovery [46]. N_s is the number of slices in 3D FFP imaging, and N is the number of projections acquired in 3D PR imaging.

Using the above equations, we calculate imaging times for a number of gradient strengths. Since one of the first human applications for MPI may be angiography in the heart or the brain, we assume a $(10\text{ cm})^3$ FOV. This FOV would be a reasonable (minimal) FOV for both anatomical regions. A 1 mm native (i.e., no deconvolution) resolution using Resovist tracer (with a 17 nm effective mean core diameter) requires a 10 T/m magnetic field gradient in x, y, and z [61, 23, 22]. Our calculations utilize a theoretical isotropic gradient for FFP systems to allow a direct imaging time comparison to FFL systems. We assume the fastest case of no pFOV overlap during scanning (i.e., β=1), and a maximum amplitude drive field strength of 7 mT in the human heart [66]. With the above parameters, the total imaging time can be estimated as $T_{2D} \approx 3.6$ s for a single slice and $T_{3D,ffp} \approx 260$ s for the entire volume. In Table 4.1, we compare these imaging times with those of decreased gradient strengths. As seen in this table, the scan time increases as the square (2D imaging) or the cube (3D imaging) of improving image resolution. This tradeoff is similar to the scan time versus system resolution tradeoff in MRI.

In Table 4.1, we also compare imaging times of 3D PR systems with a FFL. At a native resolution of $\Delta x = 1$ mm, we calculate $K_{max} \approx \frac{1}{2\Delta x} = 500$ m^{-1}. Thus, for 1 mm resolution and a $(10\text{ cm})^3$ FOV, we must acquire at least 158 projections to avoid aliasing. With $T_{2D} \approx 3.6$ s for a single projection, the total imaging time is $T_{3D,pr} \approx 560$ s. The imaging times for decreased gradient strength cases are calculated similarly, and are listed in Table 4.1. We see that the imaging times for 3D PR are within the same order of magnitude of the 3D FFP imager.

4.3 Methods

In this section, we describe a technique to rapidly acquire large 3D FOVs using projection reconstruction with sample rotation. The imaging speed of this experimental setup is limited only by magnetic field slew rates of the system (i.e., maximum amplifier voltages). This technique is general and can be extended to acquire images in human subjects, such that the imaging speed is limited only by human magnetostimulation limits.

3D Projection Reconstruction Pulse Sequence

We designed and implemented an imaging sequence for PR MPI that can be easily scaled to a magnetostimulation-limited sequence for human MPI imaging. This sequence has been modified from the sequence of the previous chapter, which used no z slow shift movement and instead relied solely on z mechanical translation [41, 39]. Mechanical translation hindered imaging speed due to inertia and maximum velocity limits of the translation stages. Here, we augmented our system to utilize z slow shift (focus) fields. The difference in imaging speed

between the two techniques is dramatic; electronic translation reduces imaging times by over an order of magnitude. This improved technique is analogous to cone-beam CT, where the FOV is rapidly imaged in a projection format while the sample (or equivalently the magnet) is rotated slowly to acquire the necessary projections for a full three-dimensional image.
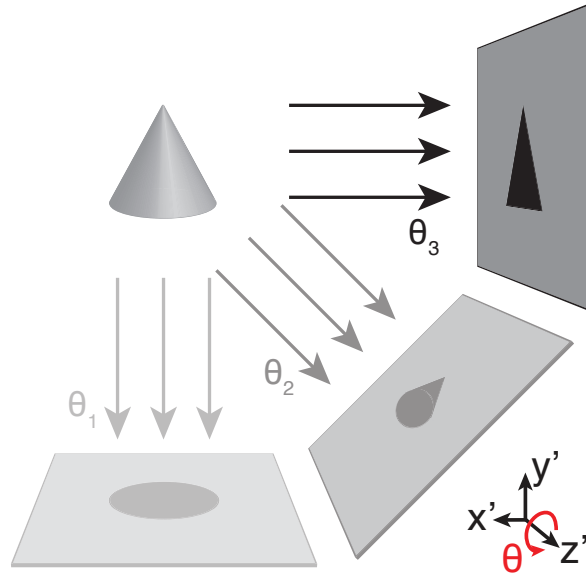
Figure 4.1: Rapid 3D imaging sequence in the sample coordinate system (x', y', z'). Multiple 2D projection images are acquired with electronic translation of the FFL. These images are taken sequentially at various angles $(\theta_1, \theta_2, \ldots \theta_N)$ using mechanical rotation of the sample around the z axis with a rotary stage. Accelerated imaging via Field Free Line (FFL) motion with time-varying slow shift magnetic fields enables acquisition of rapid tomographic 3D images in less than two minutes across a relatively large FOV.

Figure 4.1 shows a schematic overview of the imaging sequence. Two-dimensional projection images can be produced using solely magnetic translation of the FFL with x and z slow shift fields and a z drive field. The 2D FOV can be optionally extended along z using the translation stage. Following each 2D projection, the sample (or equivalently the magnet) is rotated using a mechanical rotation stage. The rotation time is small compared to the projection imaging time; implementing continuous rotation would improve imaging time by less than 10% with our current experimental system.

Figure 4.2 illustrates the FFL trajectory of each 2D projection. Figure 4.3 shows FFL trajectory waveforms that comprise the imaging sequence to produce this trajectory. We apply three simultaneous time-varying magnetic waveforms. The first, a sinusoidal drive field, rapidly scans the FFL in the z axis. The drive field elicits the MPI signal. The triangular waveforms are slowly varying magnetic fields that move the mean position of the FFL along x and z. These slow shift fields allow coverage of the full imaging FOV. The
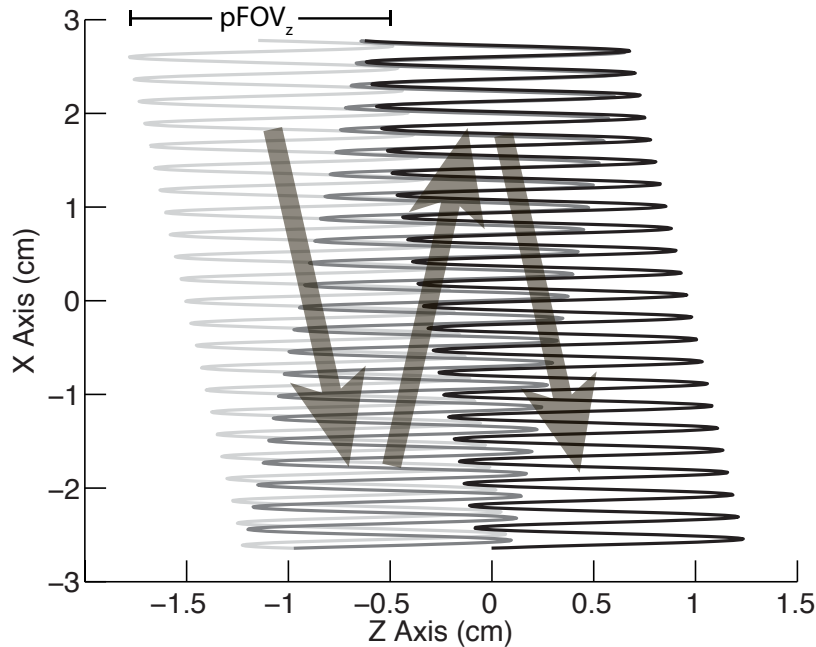
Figure 4.2: Imaging sequence of a single 2D projection scan. Each projection image is produced through the application of slowly varying fields in x and z (in scanner coordinates), and a rapidly varying drive field in z. The signal is received only along the z axis. 2D projection imaging does not require mechanical movement of the sample; however, the FOV can be optionally extended in the z direction with a translation stage. Here, a sparse trajectory is shown for illustration purposes, while the actual scanning trajectory is considerably denser.

optional z mechanical translation is used to extend the FOV along z. The final waveform in Figure 4.3 shows the angular control of the motor driven rotary table.

In our experimental imaging system, the imaging speed is limited by the current and voltage slew rates of the driving amplifiers. In a human-sized system, on the other hand, the imaging speed would be subject to the human safety thresholds for the three magnetic fields (one drive and two slow shift). Because magnetostimulation thresholds are expected to increase with decreasing diameter of the sample, we currently operate well below the magnetostimulation thresholds for small, mouse-sized samples.

Exciting the sample with a more complex drive field (e.g., Lissajous sequence) would improve the overall resolution of the system [22]; however, it would not dramatically change the imaging time of each projection. The imaging time is limited by the ability of the slow shift electromagnets to move the FFL across the full FOV for a human subject.
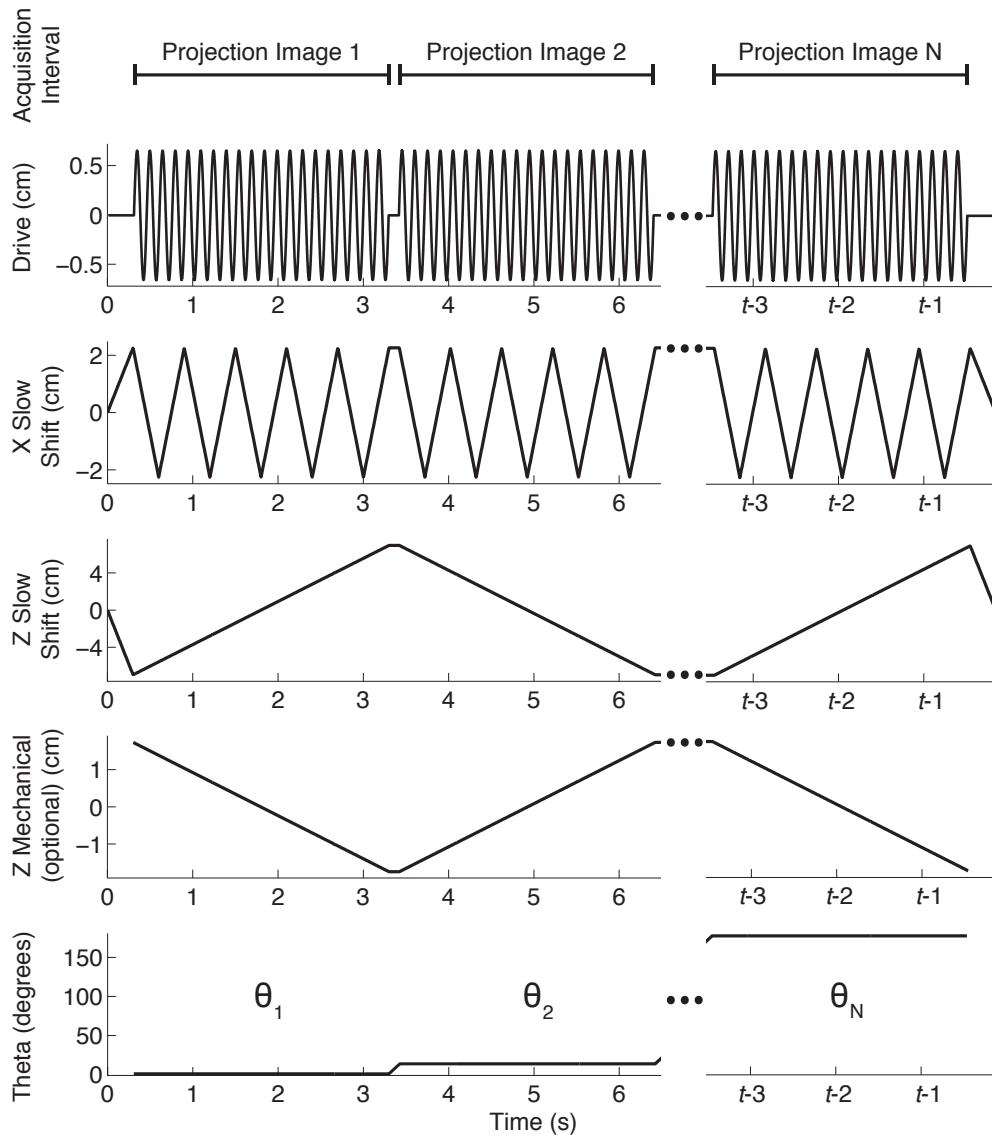
Figure 4.3: Imaging pulse sequence for electronic FFL movement (drive field in z, slow shift in x and z), mechanical rotation (θ), and mechanical z FOV extension. We simultaneously apply slowly time-varying currents in z and x to raster the FFL to produce a 2D projection image at each angle θ. The MPI signal is received continuously for each projection image. For images acquired in this chapter: total acquisition time was 1.3 min or 2.1 min with 40 projections.

Projection reconstruction MPI imaging system

Our projection reconstruction imaging system, shown in Figure 4.4, contains a FFL constructed from permanent magnets, electromagnets for slowly shifting the FFL, a drive coil, and a receiver coil. The FFL permanent magnets were assembled from 12 NdFeB permanent magnet sections, where we created two large opposing permanent magnet assemblies, each containing 6 laterally stacked magnet sections with the same magnetization orientation. This created a FFL with a 2.3 T/m selection field gradient along the x and z axes, with the FFL oriented along the y axis.
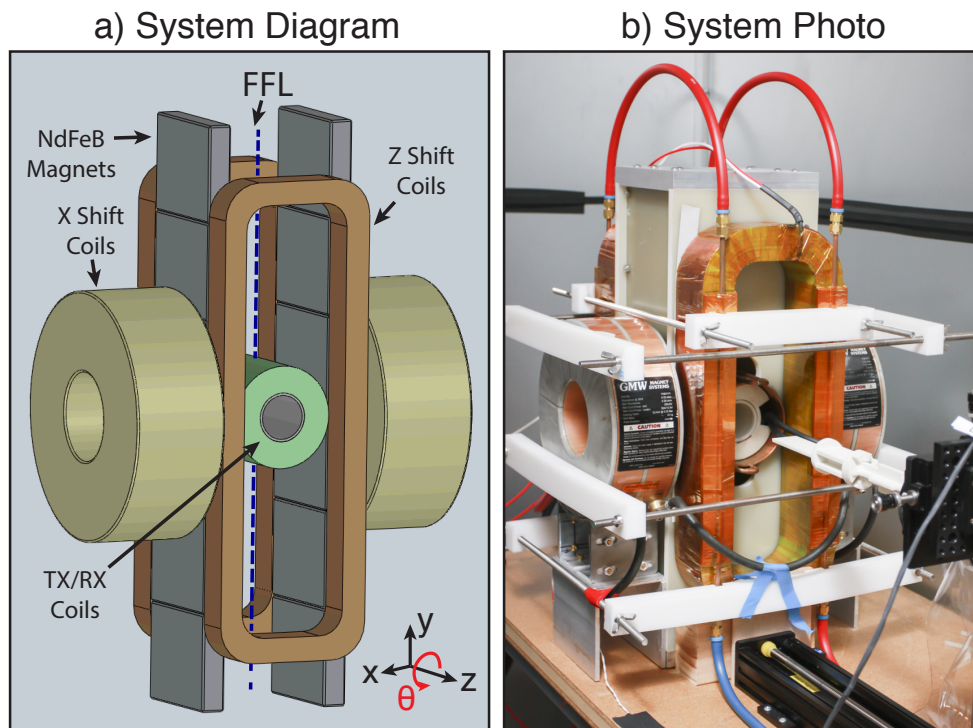
Figure 4.4: System diagram and photo of the Field Free Line (FFL) scanner for 3D Projection Reconstruction (PR) MPI. Two large opposing permanent magnet assemblies, each containing 6 laterally stacked magnet sections, create a FFL with a 2.3 T/m selection field gradient along the x and z axes, with the FFL oriented along the y axis. Slow shift coils along the z direction electronically shift the FFL to increase imaging speed 20 fold.

To slowly shift the FFL, we designed our system with two x direction electromagnets (GMW 11901111, San Carlos, CA) and two custom-manufactured z direction electromagnets. We operated these electromagnets with two switching amplifiers (Copley Controls 234). For fast translation of the FFL, a linear amplifier (AE Techron 7224 or LVC5050) drove a resonant custom-built solenoidal drive coil at 23 kHz, through a high-power passive band-pass filter. For signal reception, we wound a receiver coil in a gradiometer configuration to cancel

magnetic feedthrough from the drive coil while preserving particle signals. After the receiver coil, the receive chain consisted of a passive 23 kHz notch filter, low noise preamplifiers (SR560 and SIM911), a 500 kHz low-pass filter (SIM965), and a 40 kHz high-pass filter (SIM965). Custom software (Mathworks Matlab, Natick, MA) operates the entire system through two data acquisition cards (NI PCIe-6363, Austin, TX). A one axis translation stage with a rotation stage (Velmex, Bloomfield, NY) was used to position the sample in the imaging bore and to rotate the sample during projection reconstruction imaging.

Image acquisition and projection reconstruction
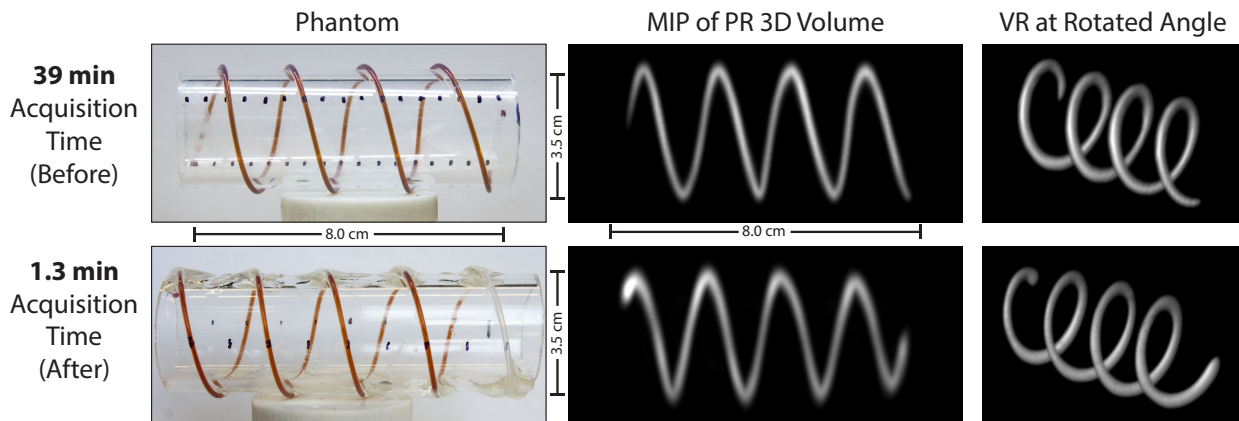
Figure 4.5: Helical tubing phantom with maximum intensity projection (MIP) and volume rendered (VR) PR MPI images comparing a slow moving table scan with 20x faster scanning using shift fields. We created a helical phantom by wrapping two pieces of 0.8 mm ID, 1.4 mm OD tubing around an acrylic cylinder. We injected 50 mM Resovist (9:1 de-ionized water and Resovist). We imaged the phantom using the pulse sequence described in Figure 4.3. The resulting dataset was maximum intensity projected and volume rendered in Osirix to produce the displayed 3D images. Top: total acquisition time: 39 min. FOV: 6 cm x 6 cm x 12 cm. 60 projections. Bottom: total imaging time: 1.3 min. FOV: 6 cm x 6 cm x 10.4 cm. 40 projections. Top row adapted from [39]. Note that the image quality and resolution are similar between the two scanning methods; however, a slight warping artifact is present in the faster dataset.

Figure 4.3 illustrates, in a simplified manner, the actual pulse sequence used for projection reconstruction images acquired in the present chapter. Images acquired in Figure 4.5 used a pulse sequence with the following parameters. For each projection, we created an oscillating drive field at 23 kHz with a 15 mT amplitude, which translates to a 1.3 cm z partial FOV in this system. A slow shift field along the x direction, operated using a 15.6 Hz, 69 mT triangle wave, covered a FOV of 6 cm along the x direction. Along the z direction, the slow shift field was a linear ramp with an 85 mT peak amplitude, which covered a 7.5 cm FOV

in 1.8 s. The z translation stage extended the FOV by 1.6 cm (in 1.8 s). The drive field, z slow shift fields, and stage movement summed to produce a total FOV of 10.4 cm along the z direction. Each image required 40 x-axis traversals to cover the entire 2D projection FOV. Using this sequence, we acquired 40 projection images at equally spaced angles to span 180 degrees. The entire imaging sequence duration was 1.3 min. The final imaging FOV was a 6 cm by 6 cm by 10.4 cm cylindrical 3D volume.

Figures 4.6 and 4.7 used the same pulse sequence with the following parameters. The drive field was the same as above, i.e., 23 kHz, 15 mT amplitude, and 1.3 cm z partial FOV. The x direction slow shift field was operated using a 3.3 Hz, 58 mT triangle wave and covered a FOV of 5 cm along the x direction. Along the z direction, the slow shift field was a linear ramp with a 69 mT peak amplitude, which covered a 6 cm FOV in 3 s. No translation stage FOV extension was used. The total FOV was 7.3 cm along the z direction. 20 x-axis traversals were used to cover the entire 2D projection FOV. 40 projection images were acquired. The entire imaging sequence duration was 2.1 min. The final imaging FOV was a 5 cm by 5 cm by 7 cm cylindrical 3D volume.

Using Equation 4.1 with $K_{max} \approx 0.15$ mm^{-1} and a $FOV_{xy} = 5$ cm, 24 projections are necessary to avoid aliasing, and 29 projections are necessary for a 6 cm FOV. Note that we acquire 40 projections to oversample and maintain image quality.

With data acquired using the above pulse sequence, we reconstructed 3D MPI tomographic images using a filtered backprojection (FBP) algorithm. At each projection angle, a 2D projection image was reconstructed using x-space reconstruction, and the baseline loss from each pFOV scan due to filtering was restored with a DC recovery algorithm [47]. We applied a receive coil sensitivity correction to each image based on a single calibration scan. Then, for all z-locations, the FBP algorithm was employed on 1D slices parallel to the x axis in each projection image to reconstruct 2D images in the xy plane, orthogonal to the axial (z) direction. A full 3D volume was obtained by stacking the xy plane images in their corresponding z position. After reconstructing an image volume, the 3D volume was exported in DICOM file format and imported into Osirix (Pixmeo, Switzerland) to create maximum intensity projection (MIP) and volume-rendered images.

Phantom experiments

To test the performance of our imaging system, we designed two phantoms to create 3D distributions of magnetic nanoparticle tracers. The first phantom (Figure 4.5) was created by wrapping tubing (ID 0.8 mm, OD 1.4 mm) filled with 50 mM Resovist (9:1 de-ionized water and Resovist) (Bayer Schering Pharma AG, Berlin, Germany), around a cylindrical piece of acrylic with a 3.4 cm outer diameter. The second phantom (Figure 4.6) was composed of three joined layers of laser-cut acrylic sheets, with the middle layer containing a pattern filled with 100 mM Fe (5-fold diluted) Resovist nanoparticles.

Mouse imaging experiments

All animal experiments were performed according to the National Research Council's Guide for the Care and Use of Laboratory animals and approved by UC Berkeley's Animal Care and Use Committee. We prepared an adult CD-1 mouse (Charles River, Wilmington, MA) for imaging by injecting 150 μL of 167 mM Fe (3-fold diluted) Resovist into the tail vein. The mouse was sacrificed 20 s post-injection, and imaged on the PR MPI system.

4.4 Results

Figure 4.5 compares the accelerated acquisition imaging below the slower original PR MPI imaging results. Each row shows photos of a helical imaging phantom adjacent to maximum intensity projection (MIP) and volume-rendered (VR) views of the acquired data set. Images of each helical tubing phantom are intended to allow comparison of image quality in both these formats and show the ability of the imager to accurately resolve continuous nanoparticle distributions in non-planar dimensions. Note how the volume-rendered images correctly show the overlap, which a projection would not show. The MIP and VR images can be rotated to any orientation. Note that the image quality and resolution remain very similar between the fast and slow scanning methods despite 20-fold speed improvement.

In Figure 4.6b, we show two acrylic imaging phantoms. In Figure 4.6a, these two phantoms are shown in their stacked imaging configuration. Figure 4.6c displays two 2D slices of the reconstructed 3D image volume at the plane of each imaging phantom. An arrow in Figure 4.6b and 4.6c points to a diagnosed blockage (due to an air bubble) in the phantom that is visible in the corresponding image slice.

The results of the mouse imaging experiments are displayed in Figure 4.7. PR MPI maximum intensity projection images from the top and side as well as a size matched photograph of the mouse are shown. The mouse was injected in a tail vein with Resovist, sacrificed after 20 seconds, and immediately imaged. The Resovist tracer can be seen in the heart, liver, and the brain of the mouse.

4.5 Discussion

While maintaining imaging quality, we have shown a 20-fold improvement in acquisition time of our PR MPI system with a new imaging sequence and new hardware. The images of Figures 4.5 and 4.6 correspond well to the tubing and acrylic phantoms. The excellent image contrast inherent in the MPI technique is evident in the post-sacrifice mouse images (Figure 4.7), where no background tissue signal is present. The imaging sequence produces images that achieve the theoretical resolution of the system [39].

Due to non-linearity in the gradient and inhomogeneity in the shift coil, a slight warping artifact is visible in the 1.3 min MIP image of Figure 4.5. This appears as a slight curvature at the edges of the image, were the edges appear compressed when compared to the center
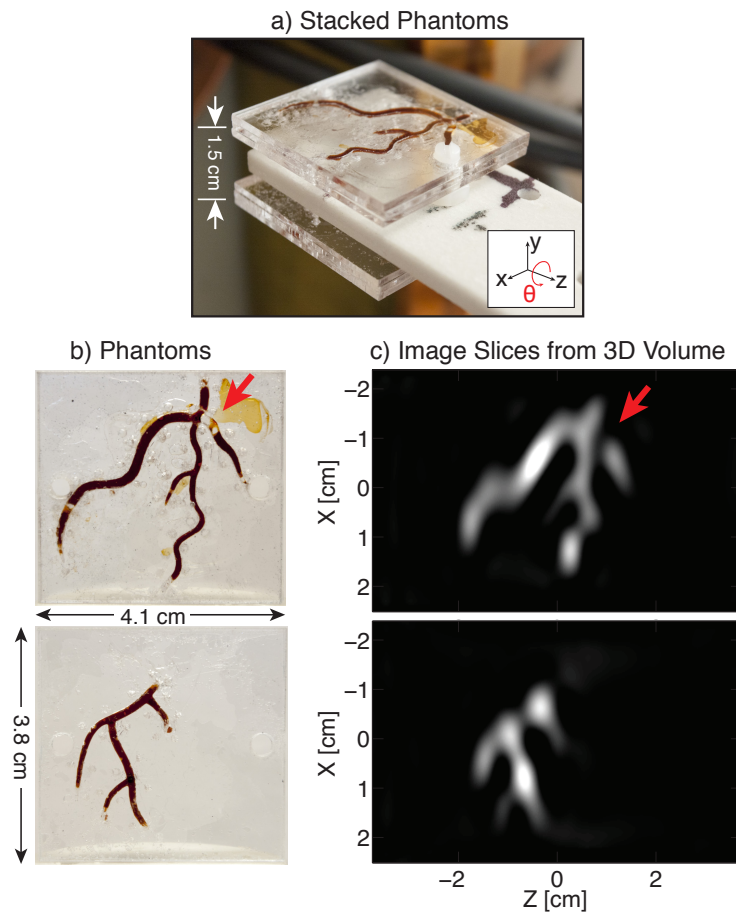
Figure 4.6: Experimental images of acrylic phantom. Following projection reconstruction, we form a full tomographic 3D image that can be sliced in any location and orientation. (a) Two planar acrylic phantoms were stacked to create a 3D Resovist distribution. (b) Two planar imaging phantoms injected with 100 mM (5x diluted) Resovist. (c) 2D image slices from the 3D PR dataset after FBP at the plane of each imaging phantom. The arrow points out a diagnosed blockage. Total imaging time of 2.1 min. FOV: 5 cm x 5 cm x 7.3 cm. 40 projections.
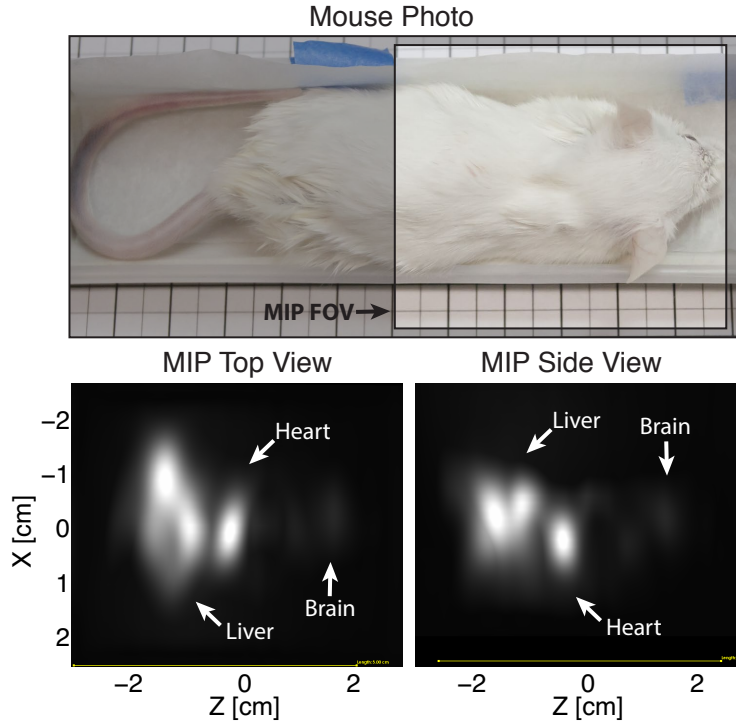
Figure 4.7: Results of mouse imaging experiments. The mouse was injected 150 μL 167 mM (3x diluted) Resovist into a tail vein. The Resovist circulated for 20 s before sacrifice. Visible are the brain, heart, and liver. Total imaging time of 2.1 min, FOV: 5 cm x 5 cm x 7.3 cm shown by unshaded area in photo. 40 projections.

of the image. This artifact is similar in concept to the gradient warping commonly seen in MRI and could easily be fixed in post-processing, but we have chosen to show the artifact here.

Use of the mechanical extension slows the acquisition time if a large translation distance is chosen. Our current translation stage operates at a constant 9 mm/s. Thus, we can only extend the FOV by 1.6 cm in the 1.8 s acquisition time in Figure 4.5.

Future improvements to our imaging system include FOV, resolution, and software enhancements. Another potential improvement is continuous rotation of the sample, as it can decrease tissue inertial motion in animal experiments [18]. The z axis slow shift coils described in this work are also capable of boosting the FFL gradient, which would enable higher resolution imaging (not shown). Alternatively, the FFL system could be redesigned with a higher gradient strength.

Similar to CT, where both cone beam CT and helical CT exist, we see two paths moving forward in PR MPI. We compare electronic FFL rotation system designs to helical CT, which uses fast gantry rotation times (e.g., 0.28 s) along with a moving table scan [43, 1, 15, 8]. Unfortunately, a system with electronic rotation requires approximately double the number

of magnets and power supplies as a system with mechanical rotation and cannot be built as a simple permanent magnet system. This is in contrast to the system presented here, which more resembles cone-beam CT imagers that are more frequently seen in radiation therapy and interventional procedures, and less so in diagnostic CT. Cone beam CT utilizes slow rotation times and obtains a large FOV with each projection image. Our PR MPI system utilizes a simple permanent magnet FFL consisting of two opposed permanent magnets. To produce a 3D image, we rotate the sample similar to micro-CT scanners [32, 29]. Alternatively, a gantry could be utilized to rotate the FFL.

In MPI, imaging speed of human-sized scanners will be limited by human safety thresholds, so there is no net improvement in imaging speed for large objects in going to a complex, rapidly rotating system with no mechanical rotation. From Table 4.1, we note that each $(10 \text{ cm})^3$ projection image will take approximately 3 seconds in a high resolution system. This relatively long projection time will lead to slow gantry rotation times for large volumes. We also note from Table 4.1, this approach will not significantly impact imaging time compared to standard 3D configurations. Furthermore, the unique flexibility of this configuration can produce real-time small-FOV 2D projection images at any angle.

From Table 4.1 and Equation A.13 and A.14, we can make two other key conclusions. First, improving the native resolution of the tracer (e.g., resolution of 1 mm in a 5 T/m gradient) results in dramatic improvements in imaging times since a smaller gradient may be used to achieve a specific resolution. Here, we refer to the native resolution without deconvolution. Deconvolution can be applied to improve the resolution of the image with a tradeoff of exponential loss of SNR [36]. Second, even improving the resolution of the tracer by four fold, a significant challenge when using iron oxide tracers [14, 13], real-time 3D full-FOV imaging of greater than 5 frames per second may not be possible at high resolution in the human heart or brain (2.5 T/m, 4 s per frame). This is not to say that real-time imaging cannot be achieved, but that it just may require the development of new acquisition techniques such as ROIs within the FOV, adaptive resolution imaging, and cine techniques.

Currently, projection reconstruction imaging is significantly slower than real time; however, there are many potential techniques for reducing the scan time for PR MPI. The most straight-forward of these techniques is to reduce the number of projections, which would undersample the object near the periphery. For reasonable reductions in sampling density, the artifacts are typically benign. If any artifacts appear due to undersampling, they usually manifest as streaking artifacts to which radiologists have become accustomed.

Fortunately, it may be theoretically possible to perform true real-time imaging (10+ FPS) across large FOVs in MPI in a 2D projection format [25]. We believe that projection imaging, or "MPI fluoroscopy," will be the standard mode of operation for angiographic applications using MPI. In the cases where 3D is required, the same imager can be used to acquire full 3D images by rotating the scanner around the bore. Further, such a hybrid instrument would have the added benefit of an order of magnitude SNR improvement.

4.6   Conclusion

We have presented a pulse sequence that theoretically produces magnetostimulation-limited images for projection reconstruction MPI. We explored imaging speed theoretical limits due to magnetostimulation and found that PR MPI does not significantly increase imaging time over a 3D FFP imager. Furthermore, PR MPI produces images with an order of magnitude higher SNR for the same imaging time. We have experimentally demonstrated hardware changes in our PR MPI system and pulse sequence changes to produce images 20-fold faster. We acquired high quality images of mice and phantoms with resolution that matches theoretical predictions. Moving forward, we anticipate that hybrid projection MPI and PR MPI systems will become the preferred MPI imaging mode because they will benefit from a combination of fast 2D imaging coupled with the option of high-sensitivity 3D imaging.

Chapter 5

MPI Reconstruction using Convex Optimization

5.1 Introduction

To reconstruct the received signal into an image in MPI, two distinct approaches to image reconstruction have been demonstrated: system function reconstruction and x-space reconstruction. The system matrix method measures or simulates how particles act inside a specific MPI system and uses this information to form a system matrix. The system matrix is then used to reconstruct an image. In contrast, x-space methods do not require any simulation or pre-characterization measurements of the MPI system and use an image space (x-space) continuity algorithm. Current 1D x-space continuity algorithms are not easily generalizable to multi-dimensional reconstructions.

Optimization approaches have been used for image reconstruction in MRI and CT to increase imaging speed, reduce image artifacts, and reduce dose [49, 9, 4, 26, 73, 44, 50, 72, 28]. For example, some techniques formulate the MRI and CT reconstruction process using *a priori* knowledge regarding the governing physics and imaging process such, continuity, non-negativity, and data consistency when imaging with multiple channels.

These same optimization approaches can be applied to MPI, where *a priori* information is utilized to improve reconstruction accuracy. In this chapter we formulate the MPI 1D, 2D, or 3D image reconstruction process as a convex optimization using knowledge that the image must be both continuous and non-negative. This new approach improves on our previous 1D x-space reconstruction which suffered from artifacts in 2D and 3D such as image banding and haze [46].

5.2 Theory

The x-space systems theory for MPI is described in [23, 22]. The MPI signal equation and point spread function (PSF) were derived using the assumption that MNPs instantaneously
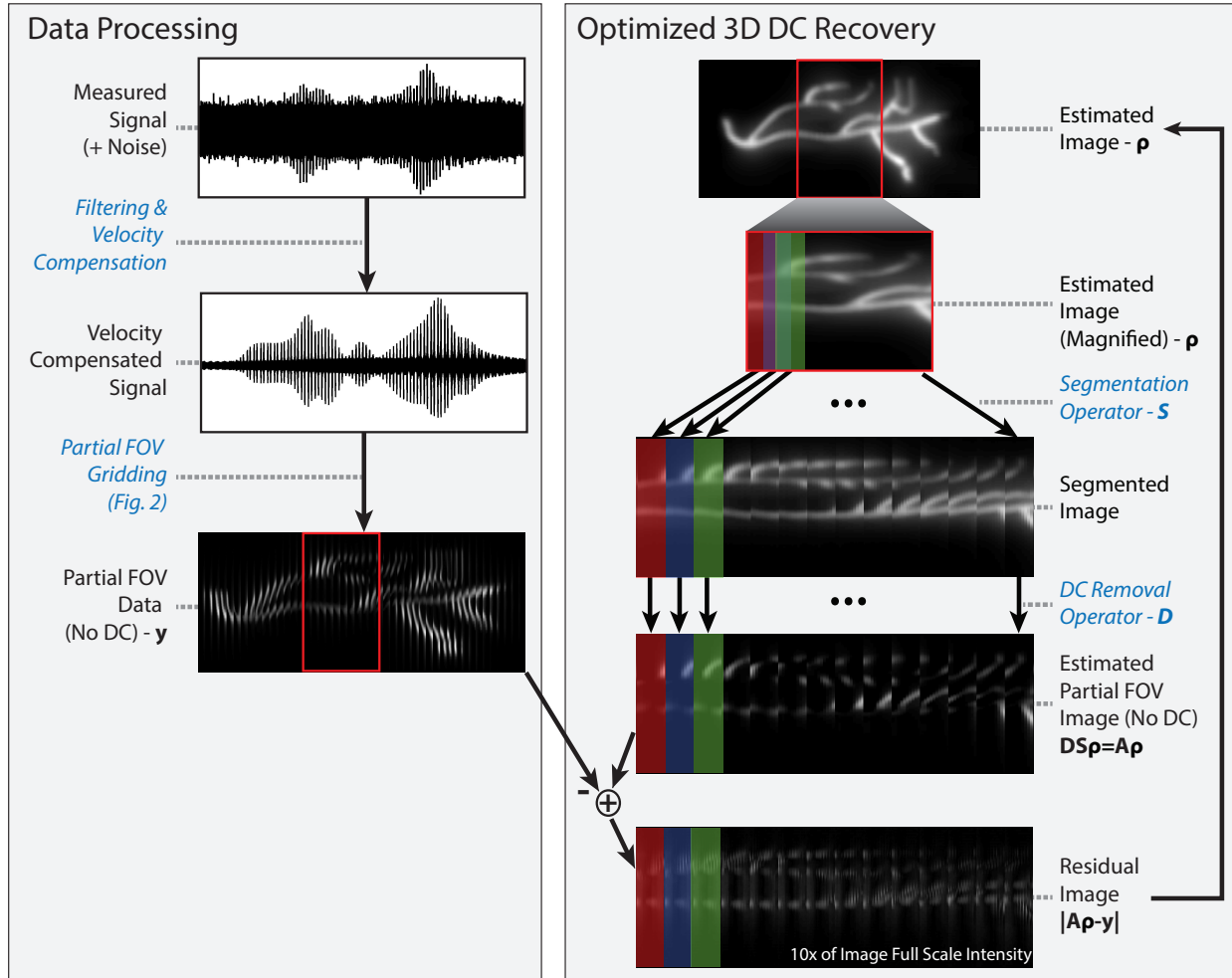
Figure 5.1: Experimental data illustrating proposed image reconstruction. **(left)** The measured signal is filtered and velocity compensated before gridding to partial field of view (FOV) images. The partial FOV images become the input to the optimization problem. **(right)** The optimization problem formulation of DC recovery is illustrated. The forward model **A** consists of the **S** and **D** operators, where **S** is the segmentation operator and **D** is the DC removal operator. The optimization problem is solved with Equation 5.3.

align with an applied magnetic field. The systems theory was then extended to include the first-harmonic direct-feedthrough filtering necessary in real MPI systems [46]. The filtered information was found to correspond to a loss of spatial DC information in the scanning direction in one dimension. Details of the previous 1D x-space data processing and image continuity algorithm are discussed in Section 5.3.

In this work, we demonstrate for the first time that the MPI reconstruction process can be improved in 2D and 3D by adding *a priori* information: the MNP distribution is non-negative, and the MNP distribution is continuous. The validity of these assumptions in MPI systems is described below.

New a priori information: 2d and 3d continuity and non-negativity

MPI images the density of magnetic nanoparticle convolved with a strictly positive point spread function; it is not possible for the MPI image to contain negative values except for those produced by noise. Thus, a physically justifiable assumption is that negative values in the final reconstructed image are non-physical.

We also know that the reconstructed MPI image must be continuous because PSF is continuous, and the system is linear and shift invariant (LSI). Because the reconstructed image is the convolution of the MNP distribution and the PSF, so long as we sample above the Nyquist limit the reconstructed image must also be continuous.

There are many ways to include this *a priori* information into the reconstruction process, including optimization, filtering, and custom algorithms. We have concentrated on fast convex optimization methods which enable rapidly solving large-scale reconstructions using modest computational hardware. Convex optimization methods can easily solve for objectives with multiple convex terms (e.g., data consistency and 3D continuity) and non-linear constraints such as non-negativity. The use of these non-linear constraints improves image quality and reconstruction robustness, thereby improving image conspicuity. Importantly, the solutions of convex optimization problems come with strong guarantees such as global optimality.

5.3   Methods

The reconstruction pipeline can be broken down into two serial processing steps: Data processing and image reconstruction (see Fig. 5.1). The data processing filters and converts the raw signal into partial FOVs. The optimized DC recovery then minimizes the residual error between the measured data and an estimated image subject to a forward model specific to a particular MPI pulse sequence as well as terms incorporating the continuity and non-negative *a priori* information. The linear operators that constitute the forward model are represented by sparse matrices and/or functions. The optimization problem is solved with

standard gradient descent based algorithms which are fast and robust. We describe these steps in detail below.

Data pre-processing and partial FOV gridding

Data pre-processing is used to remove noise from the digitized signal and to compress the data. These steps remain identical to the previously reported x-space reconstruction and are illustrated in the left column of Fig. 5.1 [23, 46].

The first steps of the data processing are filtering followed by velocity compensation. Phase correction filters reverse the phase distorted by the hardware filter chain, low pass filters remove any remaining direct-feedthrough at the fundamental frequency, and digital harmonic filtering removes signal outside a specified bandwidth of the received harmonics. Then velocity compensation is performed by normalizing the signal intensity to instantaneous field-free region (FFR) speed as required for x-space reconstruction [23, 22].

After filtering, the signal is gridded to partial FOV images as detailed in Fig. 5.2. The signal is projected onto a discrete grid using the known trajectory of the FFR and nearest-neighbor interpolation. The trajectory is redundant and creates overlapping partial FOV sub-images where one partial FOV is defined by a single traversal of the FFR.

In general, the resulting partial FOV data is missing some unknown portion of the DC component along the partial FOV horizontal axis due to direct feed-through filtering in hardware [46]. In this optimized reconstruction, each partial FOV was further filtered to remove all of the DC content along the horizontal axis for the convenience in forming the forward operation. This does not fundamentally change the DC recovery problem. The end result of the lost fundamental harmonic information and subsequent processing is the complete loss of the partial FOV DC component along one axis [61, 46].

The processed partial FOV data is significantly compressed when compared to the raw data acquired by the analog to digital converter (ADC). The original vector of raw data in the system shown later in this work contains 740 million values of data (6 GB) while the partial FOV data, $\mathbf{y}$, contains 14 million values (112 MB). This procedure reduces the size of the optimization problem by a factor of 50 while simplifying the linear forward model employed in the optimization. A vectorized partial FOV image becomes the input to the reconstruction procedure.

Linear Forward Model

A linear forward model is used to create a data consistency term necessary to solve for the 3D particle density distribution. The linear forward model describes the conversion of an image into partial FOVs with the appropriate DC signal loss due to filtering (see Fig. 5.1, right side). Thus the forward model is a simplified description of the LSI MPI system. The other aspects of the complete linear description of MPI were accounted for in the pre-processing steps.

The forward model includes two operators, segmentation $\mathbf{S}$ and DC removal $\mathbf{D}$. $\mathbf{S}$ breaks the image into overlapping partial FOV images and $\mathbf{D}$ removes the average along the hori-
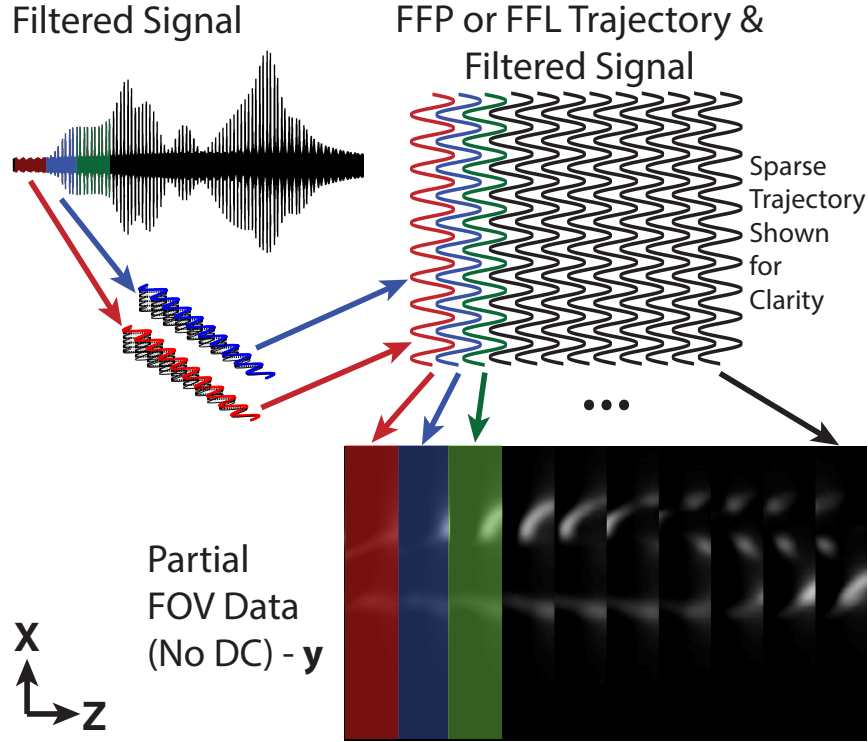
Figure 5.2: Partial field of view gridding detail. The signal is interpolated to partial field of view images using the FFR trajectory. Each x-axis traversal is broken into a separate partial FOV image. The sinusoidal pattern is formed due to the x-axis shift field and the z-axis drive field.

zontal axis of the partial FOV. This removal operation is equivalent to subtracting the DC component of the partial FOVs image. More detail is provided in Appendix A.6.

   The fundamental operators $\mathbf{S}$ and $\mathbf{D}$ are composed to form the approximate forward model of the MPI system, $\mathbf{A}$:

$$\mathbf{A} = \mathbf{DS} \tag{5.1}$$

where $\mathbf{A} \in \mathbb{R}^{m \times n}$ is a matrix, m is the product of the dimensions of the resulting image, and n is the product of the dimensions of the input partial FOV images. Both operations $\mathbf{S}$ and $\mathbf{D}$ are simple, and their composition results in an $\mathbf{A}$ matrix that is sparse and has a block diagonal-like structure. The forward model is then described by:

$$\mathbf{y} = \mathbf{A}\boldsymbol{\rho} \tag{5.2}$$

where $\mathbf{y} \in \mathbb{R}^{m}$ is the input data of vectorized partial FOVs from the scanning system and $\boldsymbol{\rho} \in \mathbb{R}^{n}$ is the column-vectorized image of MNP density.

Reconstruction via Convex Optimization Formulation

Because we have represented the imaging process as a set of linear operations, we are able to estimate the native MPI image using a convex optimization formulation, expressed below.

$$\underset{\boldsymbol{\rho}}{\text{minimize}} \quad \|\mathbf{A}\boldsymbol{\rho} - \mathbf{y}\|_2^2 + \alpha \|\boldsymbol{\rho}\|_2^2 + \beta_i \|\nabla_{\mathbf{e}_i}\boldsymbol{\rho}\|_2^2 \tag{5.3}$$

$$\text{subject to} \quad \boldsymbol{\rho} \succeq \mathbf{0}$$

where $\succeq$ is element-wise inequality, $\boldsymbol{\rho}$ and $\mathbf{y}$ are as described in (5.2), α and β_i are regularization parameters, and $\mathbf{e}_i$, $i \in \{1, 2, 3\}$ is one of the three coordinate axis basis vectors. The image non-negativity constraint improves the general robustness of the DC recovery. The Tikhonov regularization and the smoothness term, which penalizes the spatial image gradients, further stabilize the image reconstruction. Traditionally used to better condition the problem, in this case, the Tikhonov regularization also plays a role in the DC recovery by forcing the optimization problem to choose an image estimate that is not only consistent, but with the lowest total DC value (out of a nullspace containing this solution plus any arbitrary DC value). This corresponds to the most likely image, and DC recovery has been discussed theoretically in prior x-space MPI literature [46]. As noted above, the addition of smoothness and non-negativity terms are justified by *a priori* knowledge of the physics. In Appendix A.7, Equation 5.3 is reformulated as a non-negative least squares optimization problem.

Imaging Phantoms

To demonstrate the reconstruction method using our MPI system, two imaging phantoms were created. A double-helix phantom shown in Fig. 5.4 was fabricated from two 0.6 mm inner diameter tubing segments injected with magnetic nanoparticles (Micromod nanomag-MIP 78-00-102, Rostock, Germany). These tubing segments were wound around a 2.7 cm acrylic cylinder with a total length of 6.5 cm.

A coronary artery phantom 3D model with approximately human sized features was designed in SolidWorks (Dassault Systems, Maltham, MA). The arteries formed cavities in a cylindrical part. The part was printed on a 3D printer (Afinia H480, Chanhassen, MN). The 3D model is shown in Fig. 5.6. The phantom was designed with 1.8 mm by 2.3 mm maximum diameter arteries that are approximately ellipsoidal. Injection holes (shown in black) have a diameter of 1.0 mm.

The phantoms were imaged with the FFP imaging system shown in Fig. 5.3. The images were reconstructed using the formulation in Fig. 5.1. The optimization problem formulated in Equation 5.3 was solved via a proximal gradient method, Fast Iterative Shrinkage-Thresholding Algorithm (FISTA), developed in Matlab [3]. To reconstruct the image, 15 harmonics were used, for a total bandwidth of 300 kHz.

We generated deconvolved images using Wiener deconvolution. The estimated PSF returned by blind deconvolution, seeded with a calculated theoretical MPI PSF, was used in the Wiener deconvolution.
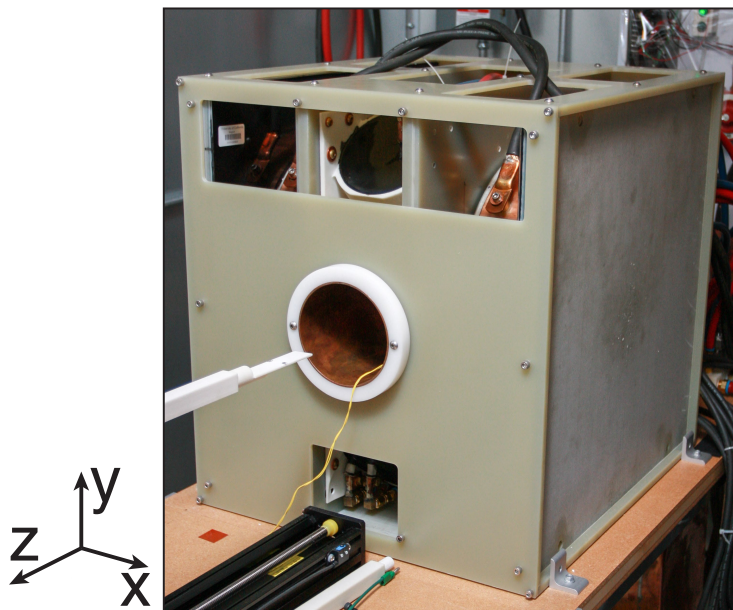
Figure 5.3: Field free point MPI system photo. This $7\,\mathrm{T\,m^{-1}}$ FFP MPI system was used to experimentally demonstrate the effectiveness of the 3D optimized reconstruction.

Figure 5.4: Experimental MPI data from a double helix phantom. The 3D dataset was reconstructed using the previous DC recovery method and the proposed method. Both datasets are shown in maximum intensity projection images with no deconvolution. Images reconstructed with the proposed method contain less background haze and fewer artifacts. The imaging phantom was constructed by wrapping two $0.6\,\mathrm{mm}$ ID tubes injected with Micromod Nanomag MIP MNPs around an acrylic cylinder of OD $2.7\,\mathrm{cm}$. The total imaging time was $10\,\mathrm{min}$ with a field of view of $4.5\,\mathrm{cm}$ by $3.5\,\mathrm{cm}$ by $7.5\,\mathrm{cm}$ (x,y,z).

5.4   Results

In Fig. 5.4 the proposed reconstruction is compared to the previous algorithm. Fewer banding artifacts are present with the proposed algorithm. No deconvolution is used.

In Fig. 5.5 the double helix phantom is shown volume rendered at three different angles to illustrate the 3D nature of the dataset. No deconvolution is used.

Experimental Data - Volume Rendered Images

Figure 5.5: Experimental data of a double helix phantom from Fig. 5.4 at different angles. The 3D volume-rendered datasets were reconstructed using the proposed method with no deconvolution. The total imaging time was 10 min with a field of view of 4.5 cm by 3.5 cm by 7.5 cm (x,y,z).

In Fig. 5.6, the proposed reconstruction is contrasted with no DC recovery and the previous algorithm. In the image with no DC recovery, the partial FOV images were averaged together to form the image with no attempt to recover the lost DC information. There are obvious dropouts. When deconvolution is used, the background haze in the image is reduced; however, note there is one dropout (marked with an arrow) in the image due to deconvolution that is not present in the reconstructed image without deconvolution.

Fig. 5.7 displays the data from Fig. 5.6 at multiple angles of rotation to demonstrate the 3D nature of the dataset. The images are volume rendered views with deconvolution.

Fig. 5.8 shows the singular values and right-singular vectors of the SVD calculated for the operator $\mathbf{A}$ to illustrate the conditioning of the proposed reconstruction. The operator was created for a 1D image reconstruction to allow the singular vectors to be shown easily. A 15 pixel overlap was used with a partial FOV width of 20. As expected, note the singular value of zero for a DC image value indicating that an image with only a DC value is in the null space of the operator. If the DC singular value is removed, the condition number of operator $\mathbf{A}$ is 5.

Table 5.1 details reduced memory requirements using matrix-free operators. All reconstruction was done on a single core of a computer with a Xenon processor and 144 GB RAM. The conversion of $\mathbf{D}$ to a matrix-free operator reduced the reconstruction time 7-fold and reduced the storage requirement of the operator to negligible amounts. For a completely matrix free operator solution, the system memory requirements then shift to the algorithm and programming language used to calculate the optimization problem, where the number
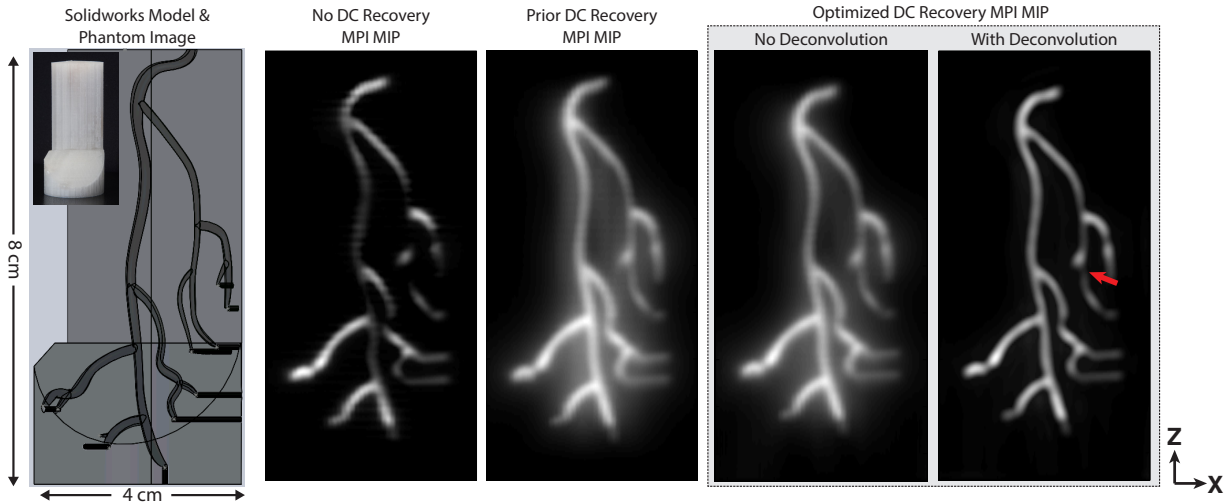
Figure 5.6: Experimental MPI data from a coronary artery phantom. Images were reconstructed with the proposed reconstruction formulation and contrasted to the previous 1D DC recovery and no DC recovery. The imaging phantom was created by 3D printing an ABS plastic coronary artery model. The reconstructed 3D dataset is shown in maximum intensity projection images. With no DC recovery, many image intensity dropouts are evident. The optimized 3D recovery contains fewer artifacts and less background haze. Light deconvolution can be used to remove remaining background haze present in the reconstructed signal. The total imaging time was 10 min with a field of view of 4.5 cm by 3.5 cm by 9.5 cm (x, y, z).

	Sparse Matrix	Matrix-Free Operator $\mathbf{D}$
RAM	32 GB	0.000 000 2 GB
Computation Time	53 min	8 min

Table 5.1: Sparse matrix versus matrix-free operator computation time and RAM requirements.

of copies of the problem input largely determine the amount of memory required.

5.5 Discussion

Image robustness to noise/artifacts are two core requirements of any imaging modality [54, 56]. To enable the acceptance of MPI, developers must produce a robust imaging system.

We see that the generalized formulation for 2D and 3D reconstruction improves the image reconstruction robustness. This is seen in Fig. 5.4, where the proposed reconstruction has
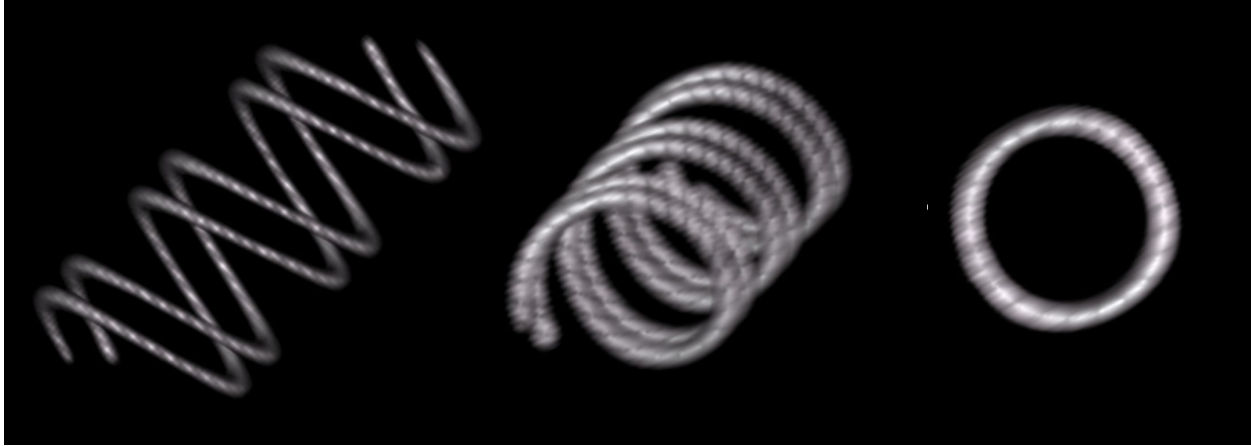
Experimental Data - Volume Rendered Images

Figure 5.7: Experimental data of a coronary artery phantom from Fig. 5.6 at different angles. The 3D volume-rendered datasets were reconstructed using the proposed method with deconvolution. The total imaging time was 10 min with a field of view of 4.5 cm by 3.5 cm by 9.5 cm (x,y,z).

improved conspicuity and reduced artifacts, including no banding and minimal haze. Banding artifacts manifest as ripples along the horizontal and vertical axes due to discontinuities between partial FOVs. Because of the *a priori* information that the image is continuous, the banding artifacts do not occur in the images reconstructed via the optimization approach, which takes advantage of image smoothness along all image axes.

As shown in Fig. 5.6, care must be taken when applying deconvolution, as deconvolution can reduce image robustness. As noted above there is one dropout in the image due to deconvolution that is not present in the actual reconstructed image as marked with an arrow. For this reason deconvolution must be applied carefully in practice to ensure the introduction of additional artifacts is minimized. Deconvolution is able to reduce the haze present with the prior algorithm, but it is not able to compensate for the banding artifacts. The banding artifact appears in the deconvolved image with the previous DC recovery, but not with the proposed DC recovery.

The robustness of a matrix inverse can be seen in the structure of the matrix's singular values. Fig. 5.8 is a reflection of this for a one dimensional reconstruction that has the same overlap properties as the full **A** matrix. The minimum singular values correspond to long straight lines in the scanning direction, which is not a structure commonly seen in
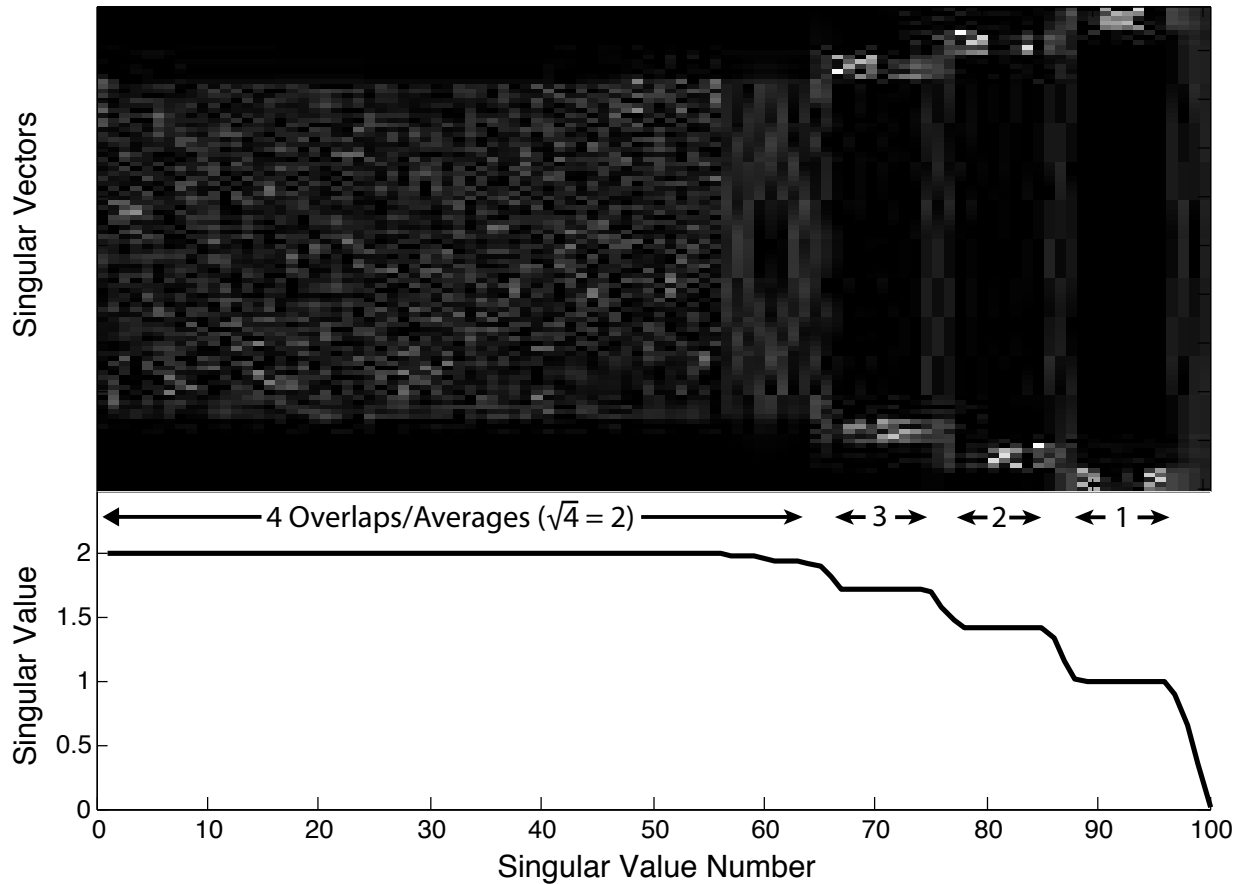
Figure 5.8: The SVD singular values and right singular vectors, $\mathbf{V}$, are calculated on $\mathbf{A}$ for a 1D problem with a 15 pixel overlap and a partial FOV width of 20. The singular vectors are shown in absolute value. The singular values demonstrate well-posed nature of the proposed reconstruction problem.

practice as most anatomical structures are tortuous. Even so, this problem can be completely resolved by exciting along two or more orthogonal axes. We note above that the condition number of the operator matrix is 5 if the DC right-singular vector is removed from the image reconstruction. Because the reconstruction process is well-formed and has just a few small singular values, the choice of regularization parameters does not have a strong effect on the resulting image.

In Fig. 5.8, the singular value magnitude varies directly with the amount of overlap in a region; the singular value plateaus are equal to the square root of the number of partial FOV overlaps. In example, for singular value indicies 1 to 64, each pixel in the central region is acquired four times in different partial FOVs so these pixels have singular values of $\sqrt{4} = 2$. Note the region of variation in the singular vectors image corresponds to the section of four overlapping partial FOVs where the singular value magnitude is 2.

The SVD confirms that our reconstruction is robust. Low singular values correspond to images with a constant value, which are due to hardware high-pass filtering of the fundamental. This is expected, as the DC recovery algorithm cannot find the correct baseline without at least one zero value. Images taken with MPI are sparse by nature, meaning most images contain at least one zero. This baseline problem is assisted by multi-dimensional excitation – an entire 2D or 3D image will have to be of some constant value to be in the null space of **A**.

Additionally, changing the overlap does not significantly alter the condition number until the overlap becomes small (a few pixels). This indicates that the choice of overlap does not change the conditioning of the problem (data not shown).

Note that the analysis done with the SVD can also drive pulse sequence design where we note that greater signal to noise ratio (SNR) efficiency may be achieved by adding additional acquisitions near the edge of the FOV to better condition the reconstruction.

The above SVD analysis shows that image reconstruction via the proposed optimization method is robust. Furthermore, the gains in image robustness from the proposed method over the previous x-space approach in terms of reduced banding and haze are significant. We anticipate that improved MPI reconstruction techniques such as optimized 3D reconstruction will be crucial for the long term acceptance of MPI in the clinic. In addition, we believe that these methods, along with advances in hardware and MNP design, will be important for reducing haze and increasing resolution. This is juxtaposed with deconvolution, which degrades SNR and can introduce artifacts.

The proposed optimization approach is extensible in many ways. In general, any new *a priori* information can easily be incorporated. It can be modified to incorporate any particular MPI pulse sequences or trajectories that may become advantageous. An example is the simultaneous reconstruction of multichannel information. The proposed approach can also be modified to include filtered backprojection for field-free line (FFL) MPI systems. In this context, compressed sensing approaches can be explored with the inclusion objective terms such as sparsity transforms: wavelet transforms, discrete cosine transforms, or Chebyshev transforms. The expansion of the formulation to include filtering and gridding steps of x-space MPI can also be explored.

5.6 Conclusion

MPI image reconstruction has been reformulated as a 3D optimization problem used in conjunction with the x-space reconstruction method. The proposed reconstruction algorithm was applied to measured data and is shown to recover the image while demonstrating robustness to noise. The reconstruction is shown to produce fewer image artifacts than the previous 1D algorithm due to use of *a priori* information, including non-negativity and image smoothness. The framework developed here has greater flexibility than the previous algorithm for future advanced applications in MPI, including generalized trajectories in x-space, projection reconstruction, filtering incorporation, and compressed sensing.

Appendix A

Appendix

A.1 FFL Rotation

An FFL magnetic field can be described using a gradient matrix in the instrument frame as

$$\mathbf{H}(\mathbf{x}) = \mathbf{Gx}$$
$$= \begin{bmatrix} -\alpha G_{zz} & G_{xy} & G_{xz} \\ G_{xy} & (\alpha - 1)G_{zz} & G_{yz} \\ G_{xz} & G_{yz} & G_{zz} \end{bmatrix} \begin{bmatrix} x \\ y \\ z \end{bmatrix},$$

where $\mathbf{x}$ is the position vector and G_{ab} is the partial derivative of the magnetic field in the a direction with respect to b. We design the FFL magnet such that $\alpha = 1$ (so the FFL lies along the y axis) and the cross terms G_{xy}, G_{xz}, and G_{yz} are zero so that the field becomes

$$\mathbf{H}(\mathbf{x}) = \mathbf{Gx} = \begin{bmatrix} -G_{zz} & 0 & 0 \\ 0 & 0 & 0 \\ 0 & 0 & G_{zz} \end{bmatrix} \begin{bmatrix} x \\ y \\ z \end{bmatrix}. \tag{A.1}$$

We then rotate the coordinate system about the z axis using the rotation matrix,

$$\mathbf{R_z}(\theta) = \begin{bmatrix} \cos\theta & -\sin\theta & 0 \\ \sin\theta & \cos\theta & 0 \\ 0 & 0 & 1 \end{bmatrix}, \tag{A.2}$$

where θ is the angle of rotation. The coordinate system after rotation is $\mathbf{x}' = \mathbf{R}_z\mathbf{x}$, and the field after rotation is $\mathbf{H}' = \mathbf{R}_z\mathbf{H}$. $\mathbf{R}_z$ is an orthogonal matrix so $\mathbf{R}_z^{-1} = \mathbf{R}_z^T$. The field is translated along the x axis in the instrument coordinate system by a homogeneous field, $\mathbf{H}_s = H_x\hat{\mathbf{i}}$. The particles are excited along the z axis by a homogeneous field, $\mathbf{H}_e = H_z\hat{\mathbf{k}}$. The field in the sample's rotated coordinate system becomes

$$\mathbf{H}'(\mathbf{x}', \theta) = \mathbf{R_z}(\mathbf{GR_z^T x'} + H_x\hat{\mathbf{i}} + H_z\hat{\mathbf{k}}).$$

The x', y', and z' axes are in the rotated (sample) coordinate system and correspond to the x, y, and z axes respectively in the instrument coordinate system. Note that in the sample's coordinate system, sample rotation and FFL rotation are equivalent operations. The trace of $\mathbf{H}'$ remains zero as required by Maxwell's equations. After simplification, each component of the magnetic field is then

$$\mathbf{H}'(\mathbf{x}', \theta) = \begin{bmatrix} -G_{zz}\cos\theta(x'\cos\theta + y'\sin\theta - H_x/G_{zz}) \\ -G_{zz}\sin\theta(x'\cos\theta + y'\sin\theta - H_x/G_{zz}) \\ G_{zz}z' + H_z \end{bmatrix}.$$

To determine where the field free line lies in space, we take the magnitude squared of the magnetic field,

$$|\mathbf{H}'(\mathbf{x}', \theta)|^2 = (G_{zz}z' + H_z)^2 \\ + G_{zz}^2(x'\cos\theta + y'\sin\theta - H_x/G_{zz})^2. \tag{A.3}$$

By inspection, we see that the field is zero at

$$z' = -H_z/G_{zz}$$

and

$$x'\cos\theta + y'\sin\theta = H_x/G_{zz}.$$

We define

$$\ell = H_x/G_{zz}.$$

Thus, the FFL lies on

$$x'\cos\theta + y'\sin\theta = \ell,$$

where ℓ [m] is the shift position perpendicular to the FFL. This is the standard notation used in CT [59].

A.2 PSF Derivation

We calculate the 2D PSF based on the normal component of the collinear FFL PSF [22]. The collinear PSF is used because the transmit excitation vector and maximum receive sensitivity are aligned (along the z axis). The normal component refers to the fact that the image axis, the x axis, is perpendicular to the transmit axis, the z axis. We begin with the expression for the multidimensional PSF,

$$\mathbf{h}(\mathbf{x}) = \dot{\mathcal{L}}\left[\|\mathbf{G}\mathbf{x}\|/H_{sat}\right]\frac{\mathbf{G}\mathbf{x}}{\|\mathbf{G}\mathbf{x}\|}\left(\frac{\mathbf{G}\mathbf{x}}{\|\mathbf{G}\mathbf{x}\|}\right)^T\mathbf{G} \\ + \frac{\mathcal{L}\left[\|\mathbf{G}\mathbf{x}\|/H_{sat}\right]}{\|\mathbf{G}\mathbf{x}\|/H_{sat}}\left(\mathbf{I} - \frac{\mathbf{G}\mathbf{x}}{\|\mathbf{G}\mathbf{x}\|}\left(\frac{\mathbf{G}\mathbf{x}}{\|\mathbf{G}\mathbf{x}\|}\right)^T\right)\mathbf{G}. \tag{A.4}$$

We then set the excitation vector along the z axis, set $\theta = 0$ so the gradient matrix is $G = diag(G_{xx}, 0, G_{zz})$, and calculate the PSF along the x axis,

$$h_{||}(x, 0, 0) = \frac{\mathcal{L}\left[|G_{xx}x|/H_{sat}\right]}{|G_{xx}x|/H_{sat}} G_{zz},$$

where we use the $||$ symbol to denote that we are using the collinear portion of the PSF.

Substituting the Langevin function, we get the following expression for the collinear 1D PSF along the x axis [22],

$$h_{||}(x, 0, 0) = \left(\frac{\coth(G_{xx}x/H_{sat})}{G_{xx}x/H_{sat}} - \frac{H_{sat}^2}{(G_{xx}x)^2} \right) G_{zz}, \tag{A.5}$$

where the unnecessary absolute values have been removed.

To determine the two dimensional PSF after projection reconstruction, we take the inverse Abel transform of the 1D PSF which is the mathematical operation for filtered backprojection [6]. This is equivalent to taking the Fourier transform and subsequently applying the inverse Hankel transform,

$$h_{pr}(r) = \mathcal{A}^{-1}\{h_{||}(x, 0, 0)\} = \mathcal{H}^{-1}\left\{ \mathcal{F}\left\{ h_{||}(x, 0, 0)\right\}\right\}.$$

The function for $h_{||}$ does not have a simple Fourier transform so we approximate the function with two Lorentzian functions,

$$\hat{h}_{||}(x, 0, 0) = \sum_{k=1}^{2} 2\beta_k \frac{1}{x^2 + \alpha_k^2}, \tag{A.6}$$

where $\alpha_1 = 3.6H_{sat}/G_{xx}$, $\alpha_2 = 27.8H_{sat}/G_{xx}$, $\beta_1 = 0.8\alpha_1^2 G_{zz}/6$, and $\beta_2 = 0.2\alpha_2^2 G_{zz}/6$. $H_{sat} = \frac{k_b T}{\mu_0 m}$ [A/m] is the field required for saturation, and $m = M_{sat}\pi d^3/6$ [T/m^3] is the magnetic moment. Parameters α_k are related to the width of the function while β_k determine the weighting of the two components. We chose the function's form from the closest match from Fourier transform tables and chose parameters α_k and β_k by fitting Equation (A.6) to Equation (A.5). Equation (A.6) is accurate to one percent RMS error as a percentage of full scale when measured within a FOV greater than or equal to 6 cm. The RMS full scale error is defined as

$$\text{error}_n = \frac{(a_n - b_n)}{\max(a)}, \tag{A.7}$$

where a_n and b_n are the values compared at each index, n. We then calculate the root mean squared value from the error vector. The projection PSF, its approximation, and the RMS full scale error are illustrated in Fig. A.1.
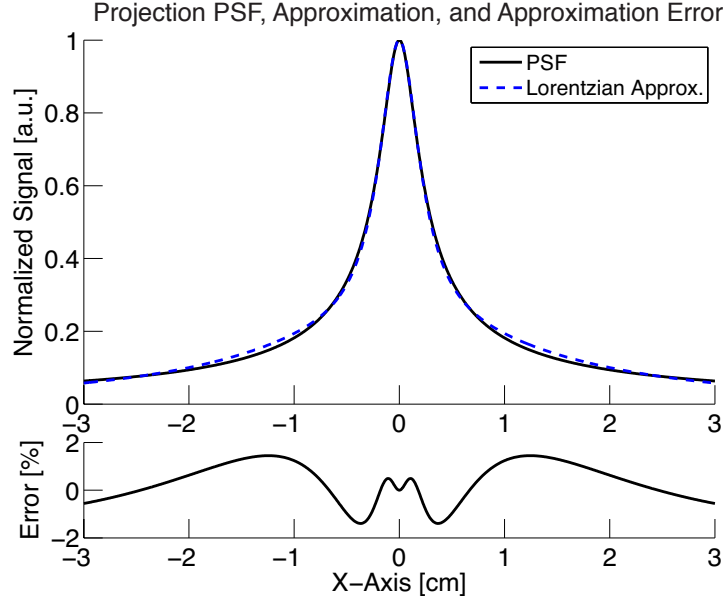
Figure A.1: Projection point spread function from Equation (A.5) and a two lorentzian approximation from Equation (A.6) as well as the error as a percentage of full scale calculated with Equation (A.7).

Using the 1D Fourier transform pair,

$$\frac{2b}{b^2 + x^2} \xrightarrow{\mathcal{F}} 2\pi e^{-b|2\pi q|},$$

the above approximation for $\hat{h}_{||}$ has a Fourier transform,

$$\hat{H}_{||}(q) \;=\; \sum_{k=1}^{2} \frac{\beta_k}{\alpha_k} 2\pi e^{-\alpha_k 2\pi q}.$$

Next, we calculate the inverse Hankel transform, which is defined from 0 to ∞; thus we drop the absolute value and use the transform pair,

$$b^{-1} 2\pi e^{-b2\pi q} \xrightarrow{\mathcal{H}^{-1}} \left(b^2 + r^2\right)^{-3/2}.$$

We arrive at the analytical approximation for the projection reconstruction PSF,

$$\hat{h}_{pr}(r) = \sum_{k=1}^{2} \beta_k \left(\alpha_k^2 + r^2\right)^{-3/2}. \tag{A.8}$$

A.3   Number of Projections

A minimum number of projections are required to avoid spatial aliasing in a projection reconstruction image. Aliasing in a PR system typically manifests as streaking artifacts. The artifacts can reduce the effective resolution of the image as well as impact the perspicuity of the images. To avoid streaking artifacts and a loss of effective resolution we can choose a sample rate that meets the Nyquist criterion. We choose system parameters such that

$$\Delta k \leq 1/FOV_{xy},$$

where Δk is the spatial frequency and FOV_{xy} is the maximum FOV in the x axis and y axis. Δk is controlled by the number of projections and how finely the projections are sampled in k-space, as illustrated in Fig. A.2.
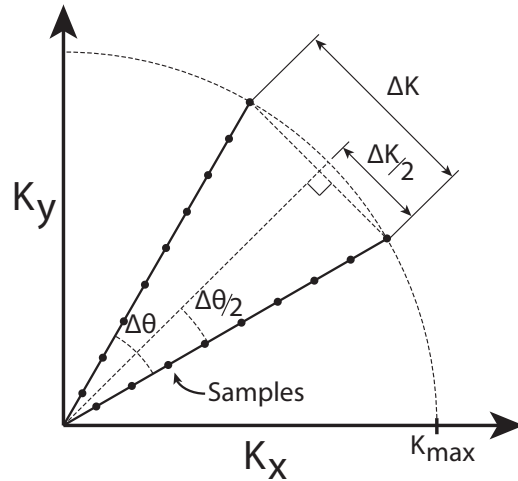
Figure A.2: The worst case distance between samples in projection reconstruction occurs at the outer radius of successive rotated projections. From these samples, we determine the minimum angular difference between projections and the maximum number of projections required to avoid aliasing according to the Nyquist criterion for projection reconstruction.

The worst-case sampling separation in k-space is

$$\Delta k = 2K_{max} \sin\left(\frac{\Delta\theta}{2}\right),$$

where K_{max} is the radius covered in k-space and $\Delta\theta$ is the angular sampling increment. Using a small angle approximation, we derive the following formula as guidance:

$$\Delta\theta < \frac{1}{FOV_{xy} \cdot K_{max}}.$$

Substituting

$$N_{proj} = \frac{\pi}{\triangle\theta},$$

where N_{proj} is the number of projections, we arrive at the formula for the number of projections needed to avoid aliasing,

$$N_{proj} > \pi \cdot FOV_{xy} \cdot K_{max}.$$

This is consistent with the result reported in Bracewell and Riddle [5].

A.4 Projection Reconstruction SNR Gain Calculation

We calculate the SNR gain of 3D projection reconstruction with a FFL as compared to 3D imaging with a FFP with equal imaging time. Here, we assume that the two systems have identical noise characteristics, pulse sequence, resolution, and gradient strength. In a simulation study, Weizenecker et al. noted that the SNR of a 3D PR image is approximately proportional to $\sqrt{N}$, where N is the number of projections acquired [76]. Here, we show how the SNR is affected by the filtered backprojection (FBP) operation. We begin by calculating the noise variance of FBP:

$$\sigma_{\mathrm{PR}}^2 = \sigma_0^2 \frac{\pi}{N} \int\limits_0^{2\pi} d\phi \int\limits_0^{K_{\max}} kdk \frac{|G(k)|^2}{k},$$

where σ_0 is the standard deviation of noise per pixel assuming gaussian random noise, k is spatial frequency, G(k) is the filter frequency response, ϕ is the angle in radians, $K_{\max}$ is the maximum radial spatial frequency of the acquired image (i.e., the total extent is $2K_{max}$). Similar calculations have been done in CT [64]. Note that filtering takes place after discretization of the acquired projection images. Hence, the spatial-frequency domain is "normalized" such that the maximum frequency is one-half cycle per pixel, i.e., $2K_{\max} = 1$. For a ramp filter $G(k) = k$, the noise variance becomes

$$\sigma_{\mathrm{PR}}^2 = \frac{2\sigma_0^2\pi^2K_{\max}^3}{3N} = \frac{\sigma_0^2\pi^2}{12N}$$

We then calculate the SNR for a PR image after filtered backprojection with a ramp filter:

$$SNR_{\mathrm{PR}} = \frac{\mu}{\sigma_{PR}} = \frac{2\sqrt{3}\mu}{\pi\sigma_0}\sqrt{N}$$

where μ is the signal mean or expected value. Similarly, the noise variance in an image acquired with a FFP can be calculated:

$$\sigma_{\mathrm{F}FP}^2 = \sigma_0^2(2K_{\max})(2K_{\max}) = \sigma_0^2$$

Thus,

$$SNR_{\mathrm{F}FP} = \frac{\mu}{\sigma_0}$$

Finally, we find

$$\frac{SNR_{\mathrm{PR}}}{SNR_{\mathrm{F}FP}} = \frac{2\sqrt{3}}{\pi}\sqrt{N}.$$

In general, the exact value of the constant multiplier before $\sqrt{N}$ depends on the shape of the filter G(k).

A.5 MPI Acquisition Time Calculation

We can calculate the optimum imaging time based on specific absorption rate (SAR) and magnetostimulation (dB/dt) limits, the two primary safety concerns when imaging human subjects using time-varying magnetic fields. Due to the frequency range in which MPI operates, magnetostimulation (and not SAR) is the dominant limitation for scanning speed in MPI [23, 66]. For human-size MPI scanners, magnetostimulation will restrict the amplitude of both the excitation (drive) field and the slow shift (focus) fields.

The drive field in MPI is typically a ~25 kHz frequency sinusoidal field. Between 5-50 kHz, the magnetostimulation threshold in the human torso is extrapolated as approximately $B_{\mathrm{th}} = 7$ mT [66]. With a $G = 10$ T/m gradient strength, which will produce 1 mm native (i.e. no deconvolution) resolution with Resovist [23, 22, 21, 20], the FOV can be calculated as: $FOV = 2B_{\mathrm{th}}/G = 1.4$ mm.

To address the limited FOV coverage of the drive subsystem, slow shift magnets [22] or focus field magnets [68] are used. These slow shift magnets slowly raster the mean position of the FFP or FFL (see Figure A.3), expanding the FOV beyond what is covered by the drive field alone. In a system with slow shift magnets, the space covered solely by the drive field (with the slow shift field disabled) is termed a "partial FOV" (pFOV) [22] or "imaging station" with multi-station reconstruction [68]. Slow shift fields also limit the acquisition time for an MPI system due to magnetostimulation limits. The ICNIRP define a maximal magnetic field slew rate of 20 T/s for pulse durations longer than a couple of milliseconds [31]. As we determine below, the slew rate causes the slow shift fields to become binding constraints on imaging time in addition to the drive field.

Generally, the total imaging time, T [s], in MPI can be calculated as

$$T = \frac{D}{v_{\mathrm{s}}}, \tag{A.9}$$

where D [m] is the total distance traveled by the Field Free Region, and v_{s} [m/s] is the slow shift field scanning rate. The total distance traveled depends on the type of drive field and slow shift field pulse sequences. Commonly a linear or Lissajous trajectory is used for the

drive field. These trajectories provide near ideal spatial coverage and are easy to calculate [75, 61].
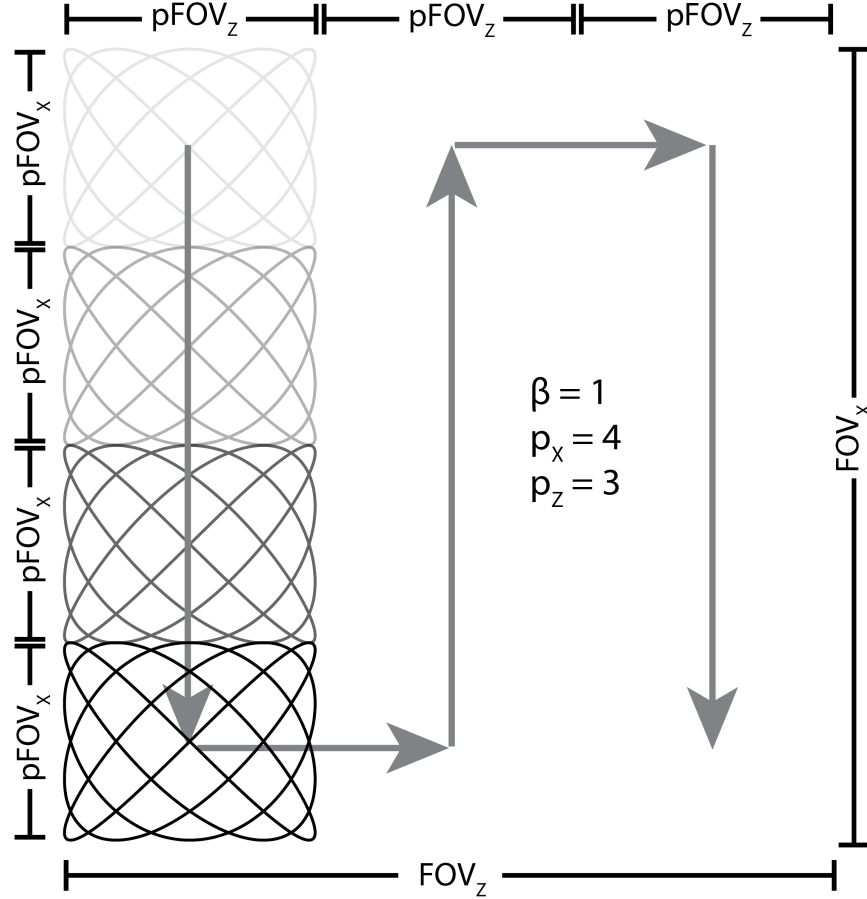
Figure A.3: Trajectory distance calculation for Lissajous pattern. The Lissajous pattern is created with two sinusoidal drive fields and is slowly rastered through the field of view with two slow shift (focus) fields.

The total distance traveled by the mean position of the field free region dominates the total imaging time assuming that (1) the time to cover the pFOV is nearly instantaneous, (2) magnetostimulation thresholds from the drive field and the slow shift fields do not affect each other, and (3) the pFOV is small relative to the total FOV (see Figure A.3). The total distance is then calculated as

$$D_{2D} \approx p_z FOV_x \qquad (A.10)$$

$$D_{3D,ffp} \approx p_z p_y FOV_x \qquad (A.11)$$

where

$$p_{\mathrm{i}} = \frac{\beta \cdot FOV_{\mathrm{i}}}{pFOV_{\mathrm{i}}}, \tag{A.12}$$

Here, 2D refers to a single slice in FFP imaging or a single projection using a FFL, and 3D refers to imaging using a FFP. FOV_{i} is the size of the Field of View along axis i, $pFOV_{\mathrm{i}}$ is the size of the partial FOV along i, p_{i} is the number of pFOVs along i, and β is a factor ($¿1$) determining the overlap extent of the pFOVs required for baseline recovery [47]. We can calculate the maximal size of the pFOV using the simple relation $pFOV = 2B_{\mathrm{th}}/G$ [m]. Accordingly, the imaging time can be estimated as

$$T_{2D} \approx \frac{\beta \cdot G_{zz} FOV_z}{2B_{\mathrm{th}}} \frac{G_{xx} FOV_x}{S_{max}}, \tag{A.13}$$

$$T_{3D,ffp} \approx \frac{\beta \cdot G_{zz} FOV_z}{2B_{\mathrm{th}}} \frac{\beta G_{yy} FOV_y}{2B_{\mathrm{th}}} \frac{G_{xx} FOV_x}{S_{max}}, \tag{A.14}$$

where $S_{max} = 20$ T/s is the maximum slew rate as described above and $\mu_0 G_{ab}$ [T/m] is the partial derivative of the magnetic field in the a direction with respect to b.

A.6   Operator Detail

The DC removal and segmentation operators are described in detail here. $\mathbf{S}$ is the segmentation operator, which breaks the image into overlapping partial FOV images:

$$\mathbf{S} = \begin{bmatrix} \mathbf{I_s} & & & & & \\ & \mathbf{I_r} & & & & \\ & & \mathbf{I_s} & & & \\ & & & \mathbf{I_s} & & \\ & & & & \mathbf{I_r} & \\ & & & & & \mathbf{I_s} \\ & & & & & & \ddots \end{bmatrix}$$

where $\mathbf{I_s}$ is an identity matrix the size of the overlap, s, between adjacent partial FOV images. $\mathbf{I_r}$ is an identity matrix the size of the $r = p - 2s$ where p is the width of partial FOV. This definition is specific to the problem with the image vectorized along the rows first with integer shift quantities. The shift value may be non-integer which interpolates between pixels (not shown).

D is the DC removal operator, which removes the average along the z-axis of the partial field of view:

$$\mathbf{D} = \begin{bmatrix} \mathbf{R} & & & \\ & \mathbf{R} & & \\ & & \ddots & \\ & & & \mathbf{R} \end{bmatrix},$$

where

$$\mathbf{R} = \mathbf{I_p} - \frac{1}{p}.$$

This operation is equivalent to subtracting the DC component in Fourier space.

Linear Operator Representation

The image reconstruction problem can be complicated by the need to construct and store very large matrices. Simply storing these matrices can be a challenge, even with considerable sparsity ($\tilde{}1{:}10^5$) present in the matrices in this work. For example, even when stored in a standard sparse form, the matrix **A** in (5.3) can require approximately $32\,\mathrm{GB}$ of memory for the 3D data sets acquired in this work.

Instead of storing sparse matrices, matrix-free operators can be utilized. Only the results of matrix vector products must be stored, while the products themselves are encoded as functions, e.g., $\mathbf{A} : X \rightarrow Y$, where X is the blurred MNP density domain and Y is the received partial FOV co-domain. These matrix-free operator methods are used in MRI, CT, and geology to reduce the storage requirements of imaging problems [50, 52, 10].

In practice, there are two challenges in converting a given matrix formulation into the equivalent matrix-free operator formulation. First, one must derive two functions: one for the linear map $(\mathbf{A}x)$ and one for the corresponding adjoint $(\mathbf{A}^T y)$. Here, matrix-free operator formulations for both the DC removal operator **D** and the splitting operator **S** and by composition **A** were developed. The functional forms can be checked for correctness by operating on the identity (returning the linear map in its finite, matrix form) and through the dot-product test [10]. As noted in the results section, going to matrix-free operator methods has significantly sped up reconstruction time and reduced RAM requirements.

A.7   Solvers

Equation 5.3 can be reformulated more generally:

$$\begin{aligned} \underset{\boldsymbol{\rho}}{\text{minimize}} \quad & \|\mathbf{T}\boldsymbol{\rho} - \mathbf{b}\|_2^2 \qquad\qquad\qquad\text{(A.15)} \\ \text{subject to} \quad & \boldsymbol{\rho} \succeq \mathbf{0} \end{aligned}$$

where

$$\mathbf{T} = \begin{bmatrix} \mathbf{A} \\ \sqrt{\alpha} \\ \sqrt{\beta_i}\nabla_{\mathbf{e}_i} \end{bmatrix} \quad \mathbf{b} = \begin{bmatrix} \mathbf{y} \\ \mathbf{0} \\ \mathbf{0} \end{bmatrix}$$

In this form, the image reconstruction problem is a basic least squares problem subject to a non-negativity constraint. Many tools for solving this basic form of non-negative least squares are available in common scientific computing platforms; however, these tools do not support using matrix-free operators to solve optimization problems. Therefore we implemented the FISTA proximal algorithms using matrix-free operators, where the proximal operator is a projection onto the non-negative orthant [3, 58]. With the solvers, we can compare the practical computational advantages or disadvantages of using matrix-free operator formulations over matrix formulations.

Bibliography

[1]   Stephan Achenbach et al. "Coronary computed tomography angiography with a consistent dose below 1 mSv using prospectively electrocardiogram-triggered high-pitch spiral acquisition." In: *European Heart Journal* 31.3 (Feb. 2010), pp. 340–6.

[2]   Tristan Barrett et al. "MRI of tumor angiogenesis." In: *Journal of Magnetic Resonance Imaging* 26.2 (Aug. 2007), pp. 235–49.

[3]   Amir Beck and Marc Teboulle. "A Fast Iterative Shrinkage-Thresholding Algorithm for Linear Inverse Problems". In: *SIAM Journal on Imaging Sciences* 2.1 (Jan. 2009), pp. 183–202.

[4]   Kai Tobias Block, Martin Uecker, and Jens Frahm. "Undersampled radial MRI with multiple coils. Iterative image reconstruction using a total variation constraint." In: *Magnetic resonance in medicine* 57.6 (June 2007), pp. 1086–98.

[5]   R. N. Bracewell and A. C. Riddle. "Inversion of Fan-Beam Scans in Radio Astronomy". In: *The Astrophysical Journal* 150 (Nov. 1967), p. 427.

[6]   RN Bracewell. "Strip Integration in Radio Astronomy". In: *Australian Journal of Physics* 9.2 (1956), p. 198.

[7]   Jeff W. M. Bulte et al. "MPI cell tracking: what can we learn from MRI?" In: *Imaging* 7965 (2011), pages.

[8]   Hersh Chandarana et al. "Abdominal aorta: evaluation with dual-source dual-energy multidetector CT after endovascular repair of aneurysms–initial observations." In: *Radiology* 249.2 (Nov. 2008), pp. 692–700.

[9]   Guang-Hong Chen, Jie Tang, and Shuai Leng. "Prior image constrained compressed sensing (PICCS): A method to accurately reconstruct dynamic CT images from highly undersampled projection data sets". In: *Medical Physics* 35.2 (2008), pp. 660–663.

[10] Jon F. Claerbout. *Earth soundings analysis: Processing versus inversion*. Cambridge, Massachusetts, USA: Blackwell Scientific Publications, 1992.

[11] Joan Connolly and Timothy G. St Pierre. "Proposed biosensors based on time-dependent properties of magnetic fluids". In: *Journal of Magnetism and Magnetic Materials* 225.1-2 (Jan. 2001), pp. 156–160.

[12]   Marlitt Erbe et al. "Experimental generation of an arbitrarily rotated field-free line for the use in magnetic particle imaging." In: *Medical Physics* 38.9 (Sept. 2011), pp. 5200–7.

[13]   R Matthew Ferguson, Amit P Khandhar, and Kannan M Krishnan. "Tracer design for magnetic particle imaging (invited)." In: *Journal of applied physics* 111.7 (Apr. 2012), 7B318–7B3185.

[14]   R. Matthew Ferguson et al. "Optimizing magnetite nanoparticles for mass sensitivity in magnetic particle imaging". In: *Medical Physics* 38.3 (2011), p. 1619.

[15]   Dominik Fleischmann and F Edward Boas. "Computed tomography–old ideas and new technology." In: *European radiology* 21.3 (Mar. 2011), pp. 510–7.

[16]   E.P. Furlani. *Permanent magnet and electromechanical devices: materials, analysis, and applications.* Academic Press, 2001.

[17]   Bernhard Gleich and Jurgen Weizenecker. "Tomographic imaging using the nonlinear response of magnetic particles." In: *Nature* 435.7046 (June 2005), pp. 1214–7.

[18]   Lee W Goldman. "Principles of CT and CT technology." In: *Journal of nuclear medicine technology* 35.3 (Oct. 2007), pp. 115–28, 115–28.

[19]   Rafael Gonzalez and Richard Woods. *Digital Image Processing.* Third Edit. New Jersey: Pearson Education, Inc, 2008, p. 954.

[20]   P. W. Goodwill et al. "Ferrohydrodynamic relaxometry for magnetic particle imaging". In: *Applied Physics Letters* 98.26 (2011), p. 262502.

[21]   Patrick W. Goodwill and Steven M. Conolly. "Experimental demonstration of x-space magnetic particle imaging". In: *Proceedings of SPIE.* Vol. 7965. 2011, pages.

[22]   Patrick W Goodwill and Steven M Conolly. "Multidimensional x-space magnetic particle imaging." In: *IEEE Transactions on Medical Imaging* 30.9 (Sept. 2011), pp. 1581–90.

[23]   Patrick W Goodwill and Steven M Conolly. "The X-space formulation of the magnetic particle imaging process: 1-D signal, resolution, bandwidth, SNR, SAR, and magnetostimulation." In: *IEEE transactions on medical imaging* 29.11 (Nov. 2010), pp. 1851–9.

[24]   Patrick William Goodwill et al. "X-Space MPI: Magnetic Nanoparticles for Safe Medical Imaging". In: *Advanced Materials* 24.28 (July 2012), pp. 3870–3877.

[25]   Patrick W Goodwill et al. "Projection x-space magnetic particle imaging." In: *IEEE transactions on medical imaging* 31.5 (May 2012), pp. 1076–85.

[26]   Mark a Griswold et al. "Generalized autocalibrating partially parallel acquisitions (GRAPPA)." In: *Magnetic resonance in medicine* 47.6 (June 2002), pp. 1202–10.

[27]   K. Halbach. "Design of permanent multipole magnets with oriented rare earth cobalt material". In: *Nuclear Instruments and Methods* 169.1 (Feb. 1980), pp. 1–10.

[28] Xiao Han et al. "Algorithm-enabled low-dose micro-CT imaging." In: *IEEE transactions on medical imaging* 30.3 (Mar. 2011), pp. 606–20.

[29] David W Holdsworth and Michael M Thornton. "Micro-CT in small animal and specimen imaging". In: *Trends in Biotechnology* 20.8 (Aug. 2002), S34–S39.

[30] William V. Houston. "The Fine Structure and the Wave-Length of the Balmer Lines". In: *The Astrophysical Journal* 64 (Sept. 1926), p. 81.

[31] International Commission on Non-Ionizing Radiation Protection (ICNIRP). "Medical magnetic resonance (MR) procedures: protection of patients." In: *Health physics* 87.2 (Aug. 2004), pp. 197–216.

[32] S M Jorgensen, O Demirkaya, and E L Ritman. "Three-dimensional imaging of vasculature and parenchyma in intact rodent organs with X-ray micro-CT." In: *The American Journal of Physiology* 275.3 Pt 2 (Sept. 1998), H1103–14.

[33] R W Katzberg and C Haller. "Contrast-induced nephrotoxicity: clinical landscape." In: *Kidney international. Supplement* 100 (Apr. 2006), S3–7.

[34] Tobias Knopp et al. "Efficient generation of a magnetic field-free line". In: *Medical Physics* 37.7 (2010), p. 3538.

[35] Tobias Knopp et al. "Generation of a static magnetic field-free line using two Maxwell coil pairs". In: *Applied Physics Letters* 97.9 (2010), p. 092505.

[36] Tobias Knopp et al. "Prediction of the spatial resolution of magnetic particle imaging using the modulation transfer function of the imaging process." In: *IEEE transactions on medical imaging* 30.6 (June 2011), pp. 1284–92.

[37] T Knopp et al. "A Fourier slice theorem for magnetic particle imaging using a field-free line". In: *Inverse Problems* 27.9 (Sept. 2011), p. 095004.

[38] T Knopp et al. "Field-free line formation in a magnetic field". In: *Journal of Physics A: Mathematical and Theoretical* 43.1 (Jan. 2010), p. 012002.

[39] Justin J Konkle et al. "Projection reconstruction magnetic particle imaging." In: *IEEE transactions on medical imaging* 32.2 (Feb. 2013), pp. 338–47.

[40] Justin Konkle, Patrick Goodwill, and Steven Conolly. "Development of a Field Free Line Magnet for Projection MPI". In: *Proc. SPIE 7965, Medical Imaging 2011: Biomedical Applications in Molecular, Structural, and Functional Imaging.* Ed. by John B. Weaver and Robert C. Molthen. Vol. 7965. Orlando, USA, Mar. 2011, pages.

[41] Justin Konkle et al. "Experimental 3D X-Space Magnetic Particle Imaging Using Projection Reconstruction". In: *Magnetic Particle Imaging: A Novel SPIO Nanoparticle Imaging Technique.* Ed. by Jörn Buzug, Thorsten M. and Borgert. Luebeck, Germany: Springer Berlin Heidelberg, 2012, pp. 243–247.

[42] R. Kötitz et al. "Determination of the binding reaction between avidin and biotin by relaxation measurements of magnetic nanoparticles". In: *Journal of Magnetism and Magnetic Materials* 194 (Apr. 1999), pp. 62–68.

[43] Bernhard Krauss, Bernhard Schmidt, and TG Flohr. "Dual source CT". In: *Dual Energy CT in Clinical Practice* (2011), pp. 11–20.

[44] Meihua Li, Haiquan Yang, and Hiroyuki Kudo. "An accurate iterative reconstruction algorithm for sparse objects: application to 3D blood vessel reconstruction from a limited number of projections". In: *Physics in Medicine and Biology* 47.15 (Aug. 2002), pp. 2599–2609.

[45] Kuan Lu, Patrick Goodwill, and Steven Conolly. "Linear and Shift Invariance of Magnetic Particle Imaging". In: *Magnetic Particle Imaging: A Novel SPIO Nanoparticle Imaging Technique*. Springer Proceedings in Physics, 2012, pp. 155–160.

[46] Kuan Lu et al. "Linearity and shift invariance for quantitative magnetic particle imaging." In: *IEEE transactions on medical imaging* 32.9 (Sept. 2013), pp. 1565–75.

[47] Kuan Lu et al. "The impact of filtering direct-feedthrough on the x-space theory of magnetic particle imaging". In: *SPIE Proceedings*. Vol. 7965. 1. Mar. 2011, pages.

[48] Min Lu et al. "FDA report: Ferumoxytol for intravenous iron therapy in adult patients with chronic kidney disease." In: *American Journal of Hematology* 85.5 (May 2010), pp. 315–9.

[49] Michael Lustig, David Donoho, and John M Pauly. "Sparse MRI: The application of compressed sensing for rapid MR imaging." In: *Magnetic Resonance in Medicine* 58.6 (Dec. 2007), pp. 1182–95.

[50] Michael Lustig and John M Pauly. "SPIRiT: Iterative self-consistent parallel imaging reconstruction from arbitrary k-space." In: *Magnetic resonance in medicine* 64.2 (Aug. 2010), pp. 457–71.

[51] Albert Macovski. *Medical Imaging Systems*. Ed. by Thomas Kailath. 1st ed. Englewood Cliffs, New Jersey: Prentice Hall, 1983, p. 256.

[52] Bruno De Man and Samit Basu. "Distance-driven projection and backprojection in three dimensions". In: *Physics in Medicine and Biology* 49.11 (June 2004), pp. 2463–2475.

[53] Peter a McCullough. "Contrast-induced acute kidney injury." In: *Journal of the American College of Cardiology* 51.15 (Apr. 2008), pp. 1419–28.

[54] C A Nienaber et al. "The diagnosis of thoracic aortic dissection by noninvasive imaging procedures". In: *The New England journal of medicine* 328.1 (Jan. 1993), pp. 1–9.

[55] Dwight G Nishimura. *Principles of Magnetic Resonance Imaging*. Stanford University, 2010, p. 226.

[56] Tara C Noone et al. "Abdominal imaging studies: comparison of diagnostic accuracies resulting from ultrasound, computed tomography, and magnetic resonance imaging in the same individual". In: *Magnetic resonance imaging* 22.1 (Jan. 2004), pp. 19–24.

[57] Q a Pankhurst et al. "Progress in applications of magnetic nanoparticles in biomedicine". In: *Journal of Physics D: Applied Physics* 42.22 (Nov. 2009), p. 224001.

[58] Neal Parikh. "Proximal Algorithms". In: *Foundations and Trends in Optimization* 1.3 (2014), pp. 127–239.

[59] Jerry L. Prince and Jonathan M. Links. *Medical imaging signals and systems*. Upper Saddle River, NJ: Pearson Prentice Hall, Jan. 2006.

[60] Jürgen Rahmer et al. "Analysis of a 3-D system function measured for magnetic particle imaging." In: *IEEE transactions on medical imaging* 31.6 (June 2012), pp. 1289–99.

[61] Jürgen Rahmer et al. "Signal encoding in magnetic particle imaging: properties of the system function." In: *BMC medical imaging* 9.1 (Jan. 2009), p. 4.

[62] J Rahmer et al. "Nanoparticle encapsulation in red blood cells enables blood-pool magnetic particle imaging hours after injection." In: *Physics in medicine and biology* 58.12 (June 2013), pp. 3965–77.

[63] G N Ramachandran and a V Lakshminarayanan. "Three-dimensional reconstruction from radiographs and electron micrographs: application of convolutions instead of Fourier transforms." In: *Proceedings of the National Academy of Sciences* 68.9 (Sept. 1971), pp. 2236–40.

[64] S J Riederer, N J Pelc, and D a Chesler. "The noise power spectrum in computed X-ray tomography." In: *Physics in medicine and biology* 23.3 (May 1978), pp. 446–54.

[65] Emine U Saritas et al. "Magnetic particle imaging (MPI) for NMR and MRI researchers." In: *Journal of magnetic resonance* 229 (Apr. 2013), pp. 116–26.

[66] Emine U Saritas et al. "Magnetostimulation limits in magnetic particle imaging." In: *IEEE transactions on medical imaging* 32.9 (Sept. 2013), pp. 1600–10.

[67] Timo F Sattel et al. "Single-sided device for magnetic particle imaging". In: *Journal of Physics D: Applied Physics* 42.2 (Jan. 2009), p. 022001.

[68] I. Schmale et al. "First phantom and in vivo MPI images with an extended field of view". In: *Imaging* 7965 (2011), pages.

[69] S A Schmitz, T Albrecht, and K J Wolf. "MR angiography with superparamagnetic iron oxide: feasibility study." In: *Radiology* 213.2 (Nov. 1999), pp. 603–7.

[70] L. A. Shepp and B. F. Logan. "Reconstructing Interior Head Tissue from X-Ray Transmissions". In: *IEEE Transactions on Nuclear Science* 21.1 (1974), pp. 228–236.

[71] Mark Supanich et al. "Radiation dose reduction in time-resolved CT angiography using highly constrained back projection reconstruction." In: *Physics in medicine and biology* 54.14 (July 2009), pp. 4575–93.

[72] Jie Tang, Brian E Nett, and Guang-Hong Chen. "Performance comparison between total variation (TV)-based compressed sensing and statistical iterative reconstruction algorithms." In: *Physics in medicine and biology* 54.19 (Oct. 2009), pp. 5781–804.

[73] Martin Uecker et al. "ESPIRiT-an eigenvalue approach to autocalibrating parallel MRI: Where SENSE meets GRAPPA." In: *Magnetic resonance in medicine* 000 (May 2013), pp. 1–12.

[74] John B. Weaver, Adam M. Rauwerdink, and Eric W. Hansen. "Magnetic nanoparticle temperature estimation". In: *Medical Physics* 36.5 (2009), p. 1822.

[75] J Weizenecker, J Borgert, and B Gleich. "A simulation study on the resolution and sensitivity of magnetic particle imaging." In: *Physics in medicine and biology* 52.21 (Nov. 2007), pp. 6363–74.

[76] Juergen Weizenecker, Bernhard Gleich, and Joern Borgert. "Magnetic particle imaging using a field free line". In: *Journal of Physics D: Applied Physics* 41.10 (May 2008), p. 105009.

[77] J Weizenecker et al. "Three-dimensional real-time in vivo magnetic particle imaging." In: *Physics in medicine and biology* 54.5 (Mar. 2009), pp. L1–L10.

[78] Yingying Zhang-O'Connor and Jeffrey a Fessler. "Fourier-based forward and back-projectors in iterative fan-beam tomographic image reconstruction." In: *IEEE transactions on medical imaging* 25.5 (May 2006), pp. 582–9.